Particle Formation from Pulsed Laser Irradiation of Soot Aggregates Studied with SMPS, TEM, NEXAFS, and Modeling

Hope A. Michelsen[a]*, Alexei V. Tivanski[b], Mary K. Gilles[b], Laura H. van Poppel[c], Mark A. Dansson[a,d], and Peter R. Buseck[c]

[a]Combustion Research Facility, Sandia National Laboratories, P. O. Box 969, MS 9055, Livermore, CA 94551-0969; [b]Chemical Science Division, Lawrence Berkeley National Laboratory, 1 Cyclotron Rd., MS 6R2100, Berkeley, CA 94720; [c]Departments of Geological Sciences and Chemistry/Biochemistry, Arizona State University, Tempe, AZ 85287-1404; [d]Now at Department of Physics, Harvey Mudd College, Claremont, CA 91711; *Send correspondence to hamiche@ca.sandia.gov

A scanning mobility particle sizer was used to measure changes in size distributions of soot particles when exposed to laser radiation at 532 or 1064 nm with fluences up to 0.8 J/cm^2. Laser-induced production of carbon nanoparticles was observed at fluences above 0.12 J/cm^2 at 532 nm and 0.22 J/cm^2 at 1064 nm. Near-edge x-ray absorption fine structure spectra showed predominantly graphitic (sp^2-hybridized) carbon in the non-irradiated particles and significantly different features in the irradiated particles. These results are consistent with differences in the fine structure between irradiated and non-irradiated samples observed by transmission electron microscopy.

OCIS codes: 350.3450 (Laser-induced chemistry), 350.4990 (Particles), 180.7460 (X-ray microscopy), 180.5810 (Scanning microscopy), 120.1740 (Combustion diagnostics)

1. Introduction

Combustion-generated soot particles are composed of small (15-50 nm diameter[1-6]) carbon spheres held together by covalent bonds to form branched-chain aggregates of varied sizes.[3,7] These small carbonaceous spheres are commonly called "primary particles", a term that in this context refers to the elementary building blocks of the aggregate without implications regarding origin, and the aggregates are referred to as "mature soot particles" to distinguish them from the smaller (~5 nm diameter) nascent particles that are initially formed. The complex structure of soot aggregates, coupled with their typical small sizes (<1 μm), makes soot detection by optical methods challenging.[8-14] The work presented here focuses on identifying laser-induced changes in aggregate morphology and fine structure, which could have an impact on implementation of laser-based soot detection schemes.

One technique that may be particularly susceptible to laser-induced particle modification is laser-induced incandescence (LII). LII is a widely used optical technique for soot detection.[15] It involves measuring the light emitted by particles heated by laser irradiation to temperatures (2500-4500 K) at which they incandesce (i.e., emit observable radiation). The signal magnitude is correlated with the particle volume fraction, whereas the signal decay rate is assumed to be associated with the primary particle size.[15-28] Accurate measurements of particle volume fraction and size are hindered by limitations in the understanding of the physical mechanisms that determine signal magnitudes and decay rates at operating temperatures and the paucity of information about the properties of soot at such temperatures. The laser fluences typically used

and temperatures attained by the particles may be sufficient to lead to significant changes in particle morphology and fine structure, which could have a substantial effect on the LII signal.

In this study, we investigated the physical and chemical changes induced in soot aggregates exposed to laser radiation at 532 and 1064 nm over a wide range of laser fluences using results from a scanning mobility particle sizer (SMPS), a transmission electron microscope (TEM), and a scanning transmission x-ray microscope (STXM) to perform near edge x-ray absorption fine structure (NEXAFS) spectroscopy. Extensive new particle production was observed to occur at fluences above 0.12 J/cm^2 at 532 nm and above 0.22 J/cm^2 at 1064 nm. Our results indicate that new particle formation proceeds via (1) vaporization of small carbon clusters by thermal or photolytic mechanisms, followed by homogeneous nucleation, (2) heterogeneous nucleation of vaporized carbon clusters onto material ablated from primary particles, or (3) both processes. These results appear to refute previous suggestions that soot aggregates break apart into primary particles during laser heating, a process we will henceforth refer to as "disaggregation". Particles retained their original morphology, fine structure, and chemical structure with laser irradiation at fluences below the threshold for new particle formation.

2. Previous Results

Previous work suggested that nanoparticles may be formed by disaggregation of soot aggregates into primary particles when heated with a laser at 1064 nm.[24] Filippov et al.[24] used LII signal decay rates to infer aggregate size distributions. These distributions tended to shift towards smaller sizes with increasing laser fluence. Based on these observations, the authors suggested that, during laser heating, electric charge accumulated on primary particles as a result of thermionic emission. They assumed that the aggregates were held together by van der Waals bonds between primary particles and hypothesized that the charge induced by the laser provided

sufficient electrostatic repulsion to overcome the van der Waals attraction between primary particles and promote disaggregation. They concluded that size distributions of primary particles could be inferred from LII measurements at intermediate and high laser fluences (> 0.3 J/cm^2).

Other studies indicated that soot particles do not readily disaggregate into primary particles at 1064 nm. Vander Wal and co-workers[29-32] presented TEM images of soot aggregates subjected to 1064 nm laser pulses. Soot samples were either first collected on copper grids and then exposed to laser radiation[29,30] or irradiated in the flame prior to collection on the grids.[31,32] Substantial changes in particle fine structure were observed. At intermediate fluences (0.3 - 0.6 J/cm^2), mass appeared to be lost primarily from the centers of the primary particles, leading to formation of interconnected shell-like spheres. At higher fluences (~0.8 J/cm^2), significant mass loss from the surfaces of the particles occurred, resulting in partial disappearance of primary particle structure. Neither individual primary particles nor their fragments were observed on the TEM grids, however, suggesting that either mass was lost predominantly via sublimation of carbon clusters or that the primary particles removed from the aggregates defied collection efforts or escaped from the TEM grids. These results are consistent with recent results from Kock et al.[33] who used an SMPS to measure aggregate size distributions before and after irradiation at 1064 nm. They did not observe a primary particle mode in the size distributions of particles irradiated at fluences between 0.1 and 0.6 J/cm^2.

Dasch[34] demonstrated that the scattering and absorption by soot decreased during laser heating at 532 nm and fluences greater than 0.2 J/cm^2, indicating a reduction in the aggregate particle size. According to model calculations that solved the energy and mass balance equations for laser heating of soot, this reduction in particle size could be explained by carbon sublimation. Dasch[34] therefore concluded that the observed changes in scattering and absorption during laser

heating were more likely explained by a decrease in primary particle size by vaporization rather than by disaggregation of the aggregate into primary particles. Witze et al.[35] and Yoder et al.[36] similarly measured changes in 532-nm[35] and 1064-nm[36] laser light elastically scattered from the particles as a result of laser heating. Both groups observed significant decreases in laser scatter at fluences above 0.2 J/cm^2 and attributed these results to particle size reduction caused by vaporization. They concluded that below 0.2 J/cm^2 mass loss was minimal. Witze et al.[35] confirmed their results with simultaneous extinction measurements. Krüger et al.[37] irradiated a sample of soot at 532 nm and observed a distortion in the size distribution measured with an SMPS at a laser fluence of 0.12 J/cm^2. They attributed this reduction in the size of particles at the larger end of the distribution upon irradiation to carbon vaporization. They did not observe enhanced volume fractions of smaller diameter particles.

Previous studies demonstrated that carbon atoms are released from soot irradiated at 193 nm[38] and that C_2 is released by irradiation at 516, 563, and 193 nm.[38-41] Using an SMPS to measure size distributions, Stipe et al.[42] observed nanoparticle production from soot aggregates exposed to 193-nm radiation. Nanoparticle formation was observed at laser fluences as low as 0.07 J/cm^2. Both mobility diameter and nanoparticle number concentration increased with increasing fluence below 0.14 J/cm^2, at which point they reached asymptotic values of ~48 nm in new particle size and ~2×10^7 cm^{-3} in number concentration. At higher fluences (between 0.18 and 0.26 J/cm^2), the mean size decreased with fluence, and the concentration of new particles was independent of fluence. Because the observed sizes of small particles varied continuously from 20 to 50 nm, the authors concluded that fragmentation of aggregates into primary particles is not the dominant mechanism for new particle formation. They hypothesized that small carbon clusters form new particles by homogeneous nucleation or by heterogeneous nucleation with

larger fragmented primary particles. Incandescence was not observed, indicating that very little of the photon energy is converted to thermal energy. At these wavelengths, production of carbon clusters and other fragments likely proceeds by direct photodissociation of covalent bonds within primary particles.

The results of Stipe et al.[42] are consistent with studies of laser interactions with bulk graphite. When irradiated with a UV laser under vacuum, graphite produces small ionic and neutral clusters. The main products are C, C_2, and C_3 and their cationic counterparts.[43-52] Small clusters initially produced are thought to form larger clusters via termolecular reactions,[53-56] and at higher pressures larger clusters have been observed.[57] The fine structure of the graphite substrate also appears to have an impact on the size of clusters produced. Evidence suggests that single-crystal (i.e., well ordered) graphite targets produce larger clusters than do amorphous carbon targets.[49,58] With laser irradiation in the visible and IR, small clusters consisting of a few carbon atoms are produced,[44,55,56,59-72] but larger clusters (with as many as 100 carbon atoms) are also commonly observed in these wavelength regions under vacuum.[46,56,61,62,73] At these wavelengths large clusters, fullerenes, and nanoparticles can be formed at higher pressures[53,54,64,74-78] or when expanded in a buffer gas into a vacuum.[65-67,79-82] Cluster growth rates via termolecular reactions should increase with pressure, thereby leading to small (60-100 nm diameter) particle formation at high pressure.[53,57,65,70,75,76,78,79,83]

In the present study, we focus on the effects on soot of laser irradiation at 532 and 1064 nm. In addition to making use of an SMPS to measure changes in electric-mobility size distributions following irradiation over a wide range of laser fluences, we use TEM and STXM images to study changes in soot morphology and fine structure and NEXAFS spectroscopy to study changes in chemical structure (carbon hybridization). The results from these studies

collectively indicate that new particles produced during laser irradiation of soot are formed by nucleation of small carbon clusters generated by sublimation or photodesorption. Nucleation proceeds homogeneously and/or heterogeneously onto larger fragments ablated by the laser. New particles appear not to be formed by disaggregation of soot aggregates into primary particles.

3. Methodology

A. Particle Generation

The experimental apparatus, shown schematically in Fig. 1, included a coflow diffusion burner, an annular silica gel diffusion dryer (TSI 3062), an atmospheric pressure flow-tube reactor with temperature and humidity probes, a cell with windows for optical access, and a scanning mobility particle sizer (TSI Model 3936L10). The SMPS includes a differential mobility analyzer (DMA, TSI Model 3085) and a condensation particle counter (CPC, TSI, Model 3025A). Soot particles were generated in the flame and cooled to ambient temperatures at atmospheric pressure. The combustion products were dried by passing through the diffusion dryer, and introduced into the SMPS after being subjected to a laser pulse at 532 or 1064 nm in the optical cell. The particles were size segregated as a function of their electric mobility diameter with the DMA and were either counted with the CPC or collected on TEM grids using an electrostatic aerosol sampler (TSI, Model 6069). Alternatively the full flow was directed onto a TEM grid or Si_3N_4 window for analysis using a STXM.

Soot was generated in an ethylene/air diffusion flame produced by a burner with a central fuel nozzle (0.5 cm in diameter) surrounded by a honeycomb structure for the coflow of air. The flow rates were maintained by mass flow controllers (MKS type 1479A for low flow and 1559A

for high flow) in the range of 0.22 - 0.26 standard liters per minute (SLM) ethylene and 27.5 SLM air. The tip of the flame was cut with a cross flow of dry air at 65 SLM to prevent complete combustion of the particles in the flame. A small fraction (~0.5%) of the total gas flow was extracted into the diffusion dryer and sent to the optical cell, where it was irradiated with a single laser shot at either 532 or 1064 nm. Gas temperature (T = 293 ± 2 K) and relative humidity (RH = 5 ± 2 %) were monitored with a thermo-hygrometer (Oakton, Model EW-35612-00) inserted through a sidearm in the flow tube.

B. Optical Setup

The optical section of the flow tube consisted of a 6-way stainless steel cross equipped with optical access windows and an SMPS sampling port. A collimated pulsed laser beam was directed into the cell through a quartz window (tilted at Brewster's angle to minimize scatter) perpendicularly to the aerosol flow. The particles were irradiated with either the fundamental (1064 nm) or second harmonic (532 nm) of an injection-seeded Nd:YAG laser (Spectra-Physics Pro-230-10), which produced pulses at a repetition rate of 10 Hz and with a duration of 10 ns at 1064 nm and 7 ns at 532 nm. The center of the Gaussian beam was passed through a 3-mm diameter ceramic aperture, which was relay-imaged to the detection region with a 1:1 positive telescope using two 1-m focal length lenses. This configuration provided a homogeneous tophat spatial profile 3 mm in diameter. The pulse energy was attenuated by use of a half-wave plate followed by two thin-film polarizers and was measured with a surface-absorbing thermal detector (Molectron Model PM10). The linear-flow velocity in the flow tube was adjusted to 6 cm/sec to ensure that particles were not subjected to multiple laser shots. The laser-beam diameter was smaller than the diameter of the aerosol flow tube, and at this flow velocity and with a 10 Hz laser repetition rate, only ~10% of the aerosol volume was irradiated.

C. TEM Imaging

For TEM analysis, soot samples were passed through an electrostatic classifier and collected on lacey carbon film on TEM grids (Electron Microscopy Sciences, LC200-Cu) using an electrostatic aerosol sampler. This sampling configuration allowed soot aggregates to be collected on the grids following segregation by electric mobility diameter. The optimal collection time was found to be 180 minutes at a flow rate of 0.3 SLM and a potential of 10 kV on the grid. The particles thus collected were imaged using a JEOL 2000FX electron microscope operated at a 200-kV accelerating voltage. Images were then analyzed to determine the fractal and geometric dimensions of soot aggregates. Particle geometric size was measured on digitized electron micrographs by fitting ellipses to the particle outlines and taking the average of the short and long axes of the best-fit ellipse as the particle diameter. A box-counting method (ImageJ 1.32j[85]) was used for the fractal analysis.

D. NEXAFS Spectroscopy Using STXM

For NEXAFS analysis, soot samples were collected on TEM grids and Si_3N_4 windows. Samples containing more and larger particles were required for NEXAFS analysis than for TEM imaging. For this reason, the DMA size filter and electrostatic aerosol sampler were not used for the NEXAFS samples. Laser-irradiated or non-irradiated particles were collected by continuously impinging aerosol flow onto the substrates at a flow rate of 0.4 SLM and collection time of 150 mins.

Carbon K-edge NEXAFS spectra of soot particles were acquired using STXM[86] on beamlines 5.3.2 and 11.0.2 of the Advanced Light Source (Berkeley, CA) in a ~0.5 atm He-filled sample chamber. The majority of the experiments were performed at beamline 5.3.2, which has a bending magnet for an insertion device and produces horizontally polarized light in plane with

the sample. For polarization-dependence measurements, a beamline with an elliptically polarized undulator insertion device (11.0.2) was used. For STXM measurements, the x-ray beam was focused with a zone plate onto the sample, and the transmitted radiation was detected. The spot size at the sample is determined by the width of the outermost zone of the zone plate, which was 35 nm for these experiments. Images were obtained by rastering the sample and collecting transmitted light as a function of sample position. Spectra at each image pixel were obtained from stacks, which are a collection of images recorded at increasing energies across the absorption edge. Carbon K-edge spectra were acquired from 278 to 320 eV with dwell times of 1-2 ms per pixel. Incident beam intensity I_0 was measured through the sample-free region of the TEM grid. The logarithm of the intensity ratio between incident and transmitted beams (expressed as a function of energy) provided the NEXAFS spectrum in units of optical density at each image pixel. The NEXAFS spectra were obtained by averaging over regions of the particles.

On coated TEM grids (holey carbon, ultrathin carbon on holey carbon support, silicon monoxide on formvar, all from Ted Pella), particles were imaged in regions where the coating was perforated, allowing simultaneous measurement of the incident radiation and measurement of the coating in a region without soot. This holey-carbon spectrum was consistent with those measured from grids without soot and is readily distinguishable from soot in thickness, spectral intensities, and peak positions. For determination of the soot spectra, the holey-carbon region was used to measure the incident radiation. Spectra from each of the support films were examined and used in a similar manner. The soot particle spectra determined this way were similar for different TEM grid coatings.

Measured optical densities (OD or absorbance) typically ranged from 0.2 to 0.8; none were greater than 1. The energy was calibrated using the absorption bands of CO_2 at 292.74 and 294.96 eV.[87] The linear pre-edge background was subtracted from each spectrum. This background arises from scattering due to species that are non-absorbing at a particular energy and was typically ~0.050 OD for both irradiated and non-irradiated soot particles. This small pre-edge absorption relative to the absorbance at higher energies (OD ~ 0.5 at 320 eV) confirmed that the primary component of the particles is carbon.

E. Model Description

The particle temperature and mass loss by carbon-cluster volatilization during laser heating were calculated using a model described in more detail elsewhere.[88] The model solves the energy- and mass-balance equations to account for particle heating by laser absorption, annealing, and oxidation and cooling by conduction to the surrounding atmosphere, radiative emission, sublimation, and non-thermal photodesorption of carbon clusters C_2 and C_3. Particle-size reduction during sublimation, photodesorption, and oxidation is also calculated. In addition, the model includes (1) temperature-dependent thermodynamic parameters for calculating sublimation, conduction, and internal energy storage by the particle; (2) wavelength-dependent optical parameters to describe absorption and emission of radiation based on a Rayleigh-Debye-Gans (RDG) approximation for aggregates; (3) convective heat and mass flow (Stefan flow) during the sublimation of multiple cluster species (C, C_2, C_3, C_4, and C_5) from the surface; (4) a thermal accommodation coefficient appropriate for high-temperature conductive cooling; (5) a conductive cooling mechanism assuming free molecular flow at low pressure and a transition regime at high pressure; and (6) the effects of annealing on absorption, radiation, sublimation, and photodesorption.

The model descriptions of cooling and mass loss by sublimation and photodesorption are the most important components of the model for calculating particle size and temperature at fluences above 0.2 J/cm^2. This part of the model is also the most complex and, in the case of photodesorption, the most uncertain. Although previous studies suggested that laser photodesorption of carbon clusters from graphite can proceed by a nonthermal mechanism,[45,47,50,53,60,65] the nature of this mechanism, including the number of photons required, is not known. Our model includes such a mechanism, assuming that it proceeds via a 2-photon process at 532 nm with a cross section and enthalpy of reaction approximated by comparing the results with time-resolved LII measurements of soot in a flame.[39] Annealing rates are calculated using an Arrhenius expression, with activation energies for interstitial migration and vacancy/defect formation derived from studies of graphitization.

All calculations are for a single primary particle and assume minimal contact between primary particles in an aggregate. Aggregation is expected to decrease conductive cooling rates via the shielding effect.[89-91] Quasi-Monte-Carlo simulations indicate that accounting for aggregation reduces the conductive cooling rate by ~30% for an aggregate of 500 primary particles,[89] and will have less of an effect for the aggregates considered here. Aggregation also influences the particle optical properties, but these are accounted for by the use an RDG approximation for absorption and emission. Although this model does not explicitly perform the calculations for an aggregate, it does provide information about the importance of mechanisms that may be responsible for fragmentation of soot aggregates into primary particles and vaporization of carbon clusters that can recondense and form carbon nanoparticles via homogeneous or heterogeneous nucleation.

4. Experimental Results

A. Laser-Induced Size and Structure Changes

Figure 2 shows the measured electric mobility size distribution of soot particles extracted from the flame (solid line). This distribution is well described by a log-normal function, where the number concentration as a function of the natural log of the particle diameter $n(\ln D)$ is given by[92]

$$n(\ln D) = \frac{N}{\sqrt{2\pi}\ln\sigma}\exp\left\{-\frac{\left[\ln\left(\frac{D}{D_0}\right)\right]^2}{2\ln^2\sigma}\right\}. \quad (1)$$

This expression can be rewritten as a function of D according to[92]

$$n(D) = \frac{N}{\sqrt{2\pi}\,D\ln\sigma}\exp\left\{-\frac{\left[\ln\left(\frac{D}{D_0}\right)\right]^2}{2\ln^2\sigma}\right\}. \quad (2)$$

Fitting the distribution in Fig. 2 to Eqn. (1) yields the following parameters (±one standard deviation): total number concentration N=2.50(±0.02)×10^6 cm^{-3}, median mobility diameter D_0=96.4(±0.4) nm, mean mobility diameter ($\langle D\rangle = D_0\exp[\ln^2\sigma/2]$)[92] of 112(±1) nm, and geometric standard deviation σ=1.727(±0.008). Figure 2 also shows distributions of the average geometric diameter (given by an average of the maximum and minimum diameters for each particle) derived from 325 measurements from each of two TEM samples collected with the electrostatic sampler after size selection with the DMA. With the DMA set to collect particles with a mobility diameter of 100 nm, the median average geometric diameter was determined to be 115(±5) nm, and for a mobility diameter of 110 nm, the median average geometric diameter was 142(±5) nm. Figure 3a shows the corresponding TEM image, which demonstrates a typical branched-chain association of primary particles. The average particle fractal dimension is 1.7, which is also typical of mature soot generated in a flame.[2,4,13,14,93-95] In Fig. 3b, the higher-

magnification image of primary particles demonstrates fine structure composed of graphite crystallites with better defined graphene (graphitic) sheets near the particle peripheries than at the centers, which is consistent with the reported fine structure of primary particles.[1,3,96-99] The soot generated and studied in our experiments is similar in morphology and size to other flame-generated soot. Some of the aggregates appeared to have less well-defined primary particles with less turbostratic graphitic order apparent in the fine structure. These particles may have been less mature and may have originated from lower in the flame.

Figure 2 also shows the mobility-size distribution of soot particles irradiated with a single laser shot at 532 nm with a fluence of 0.7 J/cm^2 (dotted line). This distribution demonstrates an additional mode of particle sizes with smaller mobility diameters; this second mode is not apparent in the distribution in Fig. 2 for the non-irradiated soot. Although there is no reason to expect that the size distributions of the new particles and the irradiated aggregate can be strictly described by a log-normal distribution, this type of probability distribution provides a good approximation for the small-mode and large-mode size distributions. The bimodal distribution shown in Fig. 2 is well-described by a sum of log-normal distributions, i.e.,

$$n(\ln D) = n_1(\ln D_1) + n_2(\ln D_2), \tag{3}$$

where n_1 represents the large-mode distribution, and n_2, the small-mode distribution, given by Eq. (1). Fitting this function to the data yields N_1=2.47(±0.09)×10^6 cm^{-3}, D_1=87.9(±2.0) nm, and σ_1=1.737(±0.037) for the large-mode distribution and N_2=2.55(±0.07)×10^6 cm^{-3}, D_2=33.6(±0.1) nm, and σ_2=1.271(±0.006) for the small-mode distribution. The total number concentration of the large-mode distribution did not change significantly upon irradiation under these experimental conditions, but the median particle size decreased, indicating a net loss of particle mass from the aggregates.

The size distribution of the aggregates thus demonstrates a small but measurable change upon irradiation. This distortion in the distribution appears as a depletion of larger particles. Figure 4 shows the distributions from Fig. 2 represented as volume concentrations, calculated as if the particles were spherical. The total particle volume (area under the curve) of the irradiated particles is ~83% that of the non-irradiated particles, i.e., the large increase in small particles does not violate conservation of mass. Because the particles are actually not spherical, this exercise will not give an accurate representation of total mass loss, but it does suggest that the change in the large-mode distribution with irradiation is probably sufficient to account for the production of new particles.

The number of new particles produced for each aggregate F_{NP} can be estimated according to

$$F_{NP} = \frac{1}{X}\frac{\int_0^\infty n_2(D')dD'}{\int_0^\infty n_0(D)dD} = \frac{1}{X}\frac{N_2}{N_0}, \quad (4)$$

where X (= 0.1) is the volume fraction of irradiated aerosol, n_0 is the number concentration of the non-irradiated sample, N_0 is the corresponding total number concentration, n_2 is the number concentration of the small-mode distribution, and N_2 is the corresponding total number concentration. Although only 10% of the sampled aerosol volume was subjected to laser radiation, the total number concentration of new particles was 1-2 times that of the original particles. A distribution of aggregates with an average size of ~100 nm produces approximately 10-20 new particles (with a median mobility diameter in the range of 19-34 nm) per irradiated aggregate with single-shot excitation at 532 nm and 0.7 J/cm^2.

Figure 5a shows the TEM image of large-mode aggregates irradiated at 1064 nm with a fluence of 1 J/cm^2. This figure demonstrates that the morphology of irradiated particles is

similar to that of the non-irradiated soot shown in Fig. 3a. The primary particles are not as regularly shaped as those that have not been exposed to the laser. These results are generally consistent with previous observations of mass loss accompanied by little change in the aggregate morphology at 1064 nm.[30-32] The fine structure of these irradiated aggregates appears to demonstrate more long-range order than observed in the non-irradiated particles (Fig. 5b). These aggregates include primary particles with denser rings or folded ribbons of carbon layers that are not perfectly spherical. In previous work[31] these structures have been identified as annealed carbon material in which small graphene sheets (2-3 nm in length) form more extensive layered structures. At high temperatures the introduction of 5- and 7-membered rings into the hexagonal structure of these graphene sheets leads to curved surfaces. Some of the images show aggregates that appear to have sections with these features and sections that are similar to the original particles, but because only 10% of the particles in the samples have been irradiated, these images may include both irradiated and non-irradiated aggregates.

Figure 6 shows representative TEM images of particles from the small mode produced by the laser at 1064 nm and 1 J/cm^2. Figure 6a presents an image of small irregularly shaped particles attached to a section of the lacey-carbon substrate. These particles appear to consist predominantly of carbon material with little or no long-range order. This material may be amorphous carbon, which is a network of carbon atoms with some short-range order (on a 1-nm length scale) but little or no long-range order exhibiting a mixture of sp^2 and sp^3 hybridization.[100-103] In addition there appear to be isolated portions of the particles that form hollow layered carbon rings, as shown in the higher-magnification image in Fig. 6b (marked with an arrow). Similar results are obtained when the particles are irradiated at 532 nm at high fluences, as shown in Fig. 6c.

To elucidate the chemical structure (carbon-bond hybridization and functional groups) of these particles, single energy STXM images and NEXAFS spectra were collected. NEXAFS spectral features arise from transitions from a core electron to an excited state and provide information about chemical hybridization and bonding. Spectra from the carbon 1s electron lie in the energy region of ~ 285 – 350 eV. Transitions from C 1s–π^* lie in the range 285 – 291 eV. Aromatic compounds exhibit a strong peak at 285 – 286 eV arising from the C 1s–π^* transition of unsaturated C=C bonds. Additional transitions from functionalized aromatic groups, such as carbonyl groups, lie in the range 286 – 288 eV and may overlap with the C 1s–σ^* transitions of C-H or CH_2, which begin around 287 eV. Peaks arising from transitions to σ^* are usually broader than the π^* peaks and are superimposed on the photoionization continuum.

Representative STXM images of non-irradiated soot particles and particles irradiated at 532 nm and 0.8 J/cm^2 are shown in Fig. 7. Figure 7a shows an agglomerate of soot aggregates. Such agglomerates likely formed *in situ* during the sampling process. The irradiated particles (Fig. 7b) appear to be more compact, thicker, and denser. Such particles were not observed in the non-irradiated or low-fluence samples. Although only ~10% of the sample was estimated to be irradiated, particles similar to those shown in Fig. 7a were not observed for samples irradiated at high fluences. This observation implies preferential collection of irradiated particles for some reason we do not understand. Furthermore, these particles were not segregated by electric mobility diameter prior to collection. The flow impinging on the substrate thus included both small and large mode particles from the irradiated distribution; because an electrostatic classifier was not used to collect the particles, sampling in this flow likely favored collection of the larger mode aggregates. The thickness of each sample was calculated from the atomic scattering factors[104] assuming a density of 1.8 g/cm^3. Thicknesses were typically ~25 nm for the non-

irradiated and low-fluence samples, whereas the laser-irradiated particles were uniform in thickness and were typically ~85 nm thick.

Figure 8 shows representative normalized spectra from a non-irradiated sample and from a sample irradiated at 532 nm with a fluence of 0.8 J/cm^2. Non-irradiated soot aggregates have a spectrum (Fig. 8, dotted line) similar to graphite, with a strong contribution from an sp^2 component.[102,103,105] For comparison, the magic angle spectrum of highly oriented pyrolytic graphite (HOPG) extracted from Lenardi et al.[106] is shown in Fig. 8 (dashed line). The graphite spectrum exhibits a strong peak at ~285.3 eV, which is attributed to the 1s-π^* transition of aromatic carbon, and a transition at 292 eV, which corresponds to a 1s-σ^* carbon transition with enhancement from a sharp exciton transition at 291.7 eV.[105,107-109] The exciton resonances have long lifetimes and as a result are very narrow.[110]

The NEXAFS spectrum of non-irradiated soot particles (dotted line) shows absorption features similar to those of HOPG. As noted above, the strong absorptions in the π^* (285.3 eV) and σ^* (292.8 eV) regions point to the dominance of graphite-like sp^2 carbon. The linewidths of both π^* and σ^* transitions are broader than those of HOPG, however, indicating additional π^* (and σ^*) resonances in the region between 286 and 290 eV. These differences between the HOPG and soot spectra are attributable to contributions from non-carbonaceous moieties known to be part of combustion-generated particles.[3,111,112] Resonances from C=O (287.4 eV), C-H (288.7 eV), and C-OH (290 eV)[110,113] can account for the additional absorption in the 286-290 eV region.

Particles irradiated with 0.8 J/cm^2 at 532 nm (Fig. 8, solid line) have a distinctly different spectrum from either HOPG (magic-angle spectrum) or the non-irradiated sample. The strength of the 1s-π^* absorption is reduced, but the material exhibits a strong exciton at 291.7 eV. The

appearance of the exciton in the spectrum of laser-irradiated particles could indicate the presence of some short-range order, which could be attributable to formation of annealed structures, such as those shown in Figs. 6b and 6c. Such short-range order (on a length scale of ~1 nm) is also consistent with amorphous carbon, which may have small regions of clustering of sp^2- and sp^3-bonded carbon atoms.[100-103] Hence, the absorption features suggest a less graphitic structure (relative to non-irradiated aggregates) but, nevertheless, demonstrate short-range order, as indicated by sharp exciton absorption.

The relative amount of graphitic sp^2 carbon in irradiated and non-irradiated soot samples can be estimated from the ratio of the area under the 1s-π^* peak ($A_{C=C}$) to the overall area of the spectrum in the region between 280 and 310 eV ($A_{280\text{-}310}$) according to:[106]

$$f_{sp^2} = \frac{A_{C=C}}{A_{280-310}}. \tag{5}$$

Following Lenardi et al.,[106] f_{sp^2} was referenced to the corresponding ratio for the HOPG (magic-angle spectrum) sample, assuming a 100% abundance of sp^2 carbon in HOPG:

$$f_{sp^2}^{soot} = \frac{A_{C=C}}{A_{280-310}} \frac{A_{280-310}^{HOPG}}{A_{C=C}^{HOPG}}. \tag{6}$$

The area under the spectrum $A_{280\text{-}310}$ was obtained by numerical integration of the experimental data, whereas the area under the π^* peak $A_{C=C}$ was calculated by fitting the 1s-π^* transition to a Gaussian function,[110] i.e.,

$$I_\pi = H_0 \exp\left[-\frac{1/2(E-P_0)^2}{\left(\Gamma/c\right)^2} \right], \tag{7}$$

and integrating I_π. In Eq. 7, H_0 is the height of the Gaussian peak, E is the photon energy, P_0 is the position of the peak, Γ is the full width at half maximum, and c is a constant $c = 2\times(\ln 4)^{1/2}$.

From Eq. 6, the average fraction of sp^2-hybridized carbon was estimated to be 72% for the non-irradiated soot particles and 21% for the particles irradiated at 532 nm with a fluence of 0.8 J/cm^2. The estimated uncertainty is ±5%. This latter value is consistent with the composition of amorphous carbon films deposited at room temperature.[103] These results suggest significant changes in the carbon bonding in irradiated samples.

Alternatively, the NEXAFS spectrum of the irradiated particles shown in Fig. 8 (solid line) could arise from formation of an oriented carbonaceous material with polarization-dependent spectral intensities. The spectra of the irradiated particles exhibit a decrease in the 1s-π^* absorption strength at 285.3 eV as compared to the non-irradiated samples. Similar decreases can be observed in HOPG spectra when measured with the sample rotated out of plane with linearly polarized light at ~30° angle of incidence.[110] In addition, a corresponding increase in the transition intensity of the 1s-σ^* carbon transition at 292.8 eV should be apparent for the out-of-plane sample. With this orientation, the ratio of the peak intensity at 285.3 eV to that at 292.8 eV can vary by over an order of magnitude with changes in polarization. We did not observe any significant increases in the intensity of the 1s-σ^* carbon transition for the irradiated particles. Therefore, it appears that the irradiated particles were not fortuitously aligned parallel to the substrate surface, and the decrease in the intensity of the aromatic carbon (285.3 eV) transition is not simply related to the particle alignment. In addition, to test for polarization-dependent spectral intensities, spectra were collected from 8 different particles from the sample irradiated at 532 nm with 0.8 J/cm^2. Variations in the spectral intensities were on the order of a few percent. The ratio of the peak at 285.3 eV to that at 292.8 eV was measured on a single region of this sample with (0.29) vertical, (0.32) horizontal, and (0.27) circularly polarized light. The lack of

significant variation in the peak intensities for different particles supports the lack of variability in the spectra with polarization and implies that the carbon is not highly oriented.

For the non-irradiated samples, spectra were averaged over a region of the sample; hence long-range order, if any, would be averaged out in the measured spectrum. Although no polarization dependence was anticipated, analogous measurements on the non-irradiated samples yielded values of 0.71 (vertical), 0.74 (horizontal), and 0.67 (circular). This variation indicates the uncertainty of the measurement rather than significant changes in peak intensities.

Although we are unable to definitively identify a mechanism for the differences observed in the NEXAFS spectra between non-irradiated and those irradiated at 0.8 J/cm^2, the significantly altered spectra suggest either formation of new particles or annealing as a result of laser irradiation. This conclusion is consistent with the TEM images of irradiated particles (Fig. 6), which demonstrate isolated regions of carbon with relatively large graphene sheets together with regions where such sheets are not evident.

B. Fluence Dependence of New Particle Formation

The aerosol mobility-size distributions were measured as a function of laser fluence at 532 and 1064 nm. Figure 9 demonstrates the effect of laser fluence on the number concentration and size of small particles produced during laser irradiation at 532 nm. The solid lines in Fig. 9 represent the best fits to the particle size distributions of a sum of two log-normal distributions, i.e., Eq. (3). The parameters derived from this analysis are given in Table 1. The full set of experimental data for 532-nm irradiation is plotted in Fig. 10 in the form of a 3-D graph of the measured particle size distributions as a function of mobility diameter (X-axis) and laser fluence (Y-axis). The data show that small particles increase in size and number density with increasing fluence and reach a plateau in size and number concentration at higher values. Analogous results were

observed for 1064-nm excitation, although the plateau regions in particle number concentration and size were not reached.

The median sizes of the small-mode and large-mode distributions are shown as a function of fluence in Fig. 11a. The small-mode distribution increases with fluence at values above ~0.12 J/cm^2 for 532-nm irradiation and ~0.22 J/cm^2 for 1064-nm irradiation. Particles with a median size below 8 nm were not observed at either wavelength. At 532 nm the particle size becomes independent of fluence above ~0.5 J/cm^2. Such a plateau was not observed at 1064 nm at the fluences used in this study. The median particle size of the large-mode distributions starts to decrease with fluence at the value where new particle formation becomes observable. The median size of this mode continues to decrease at fluences below the intermediate values of ~0.3 J/cm^2 for 532-nm irradiation and ~0.55 J/cm^2 for 1064-nm irradiation and increases with fluence at higher values. The behavior with fluence of the large-mode particles is mirrored by the total number concentration of these particles (shown in Fig. 11b). At fluences above the threshold for new particle formation, the total volume of large-mode particles decreases with increasing fluence.

Figures 12 and 13 show TEM images of large-mode aggregates irradiated at 1064 and 532 nm at intermediate fluences. Aggregates irradiated at 1064 nm and 0.24 J/cm^2 (Fig. 12) look similar to the non-irradiated particles (Fig. 3). The aggregate morphology does not change when irradiated at this wavelength and fluence, as demonstrated in Fig. 12a, and most of the particles appear to have the same polycrystalline graphitic fine structure, as shown in Fig. 12b. Aggregates irradiated at 532 nm and 0.3 J/cm^2 (Fig. 13), however, demonstrate features similar to those observed in aggregates irradiated at 1064 nm and 1 J/cm^2 (Fig. 5). More long-range order is apparent in the fine structure, which demonstrates layered carbon rings or folded

ribbons. The nanoparticles produced under these conditions (Fig. 14) are similar in structure to those produced at higher fluences (e.g., Fig. 6). Figure 14 shows representative nanoparticles produced by laser irradiation at 1064 and 532 nm at intermediate laser fluences. In many of the particles generated, less long-range order is apparent than in the non-irradiated particles. In the case of 1064-nm irradiation at 0.24 J/cm^2 (Fig. 14a), small sections of graphitic structure are visible (circled). With 532-nm irradiation at 0.3 J/cm^2 some of the new particles have no apparent long-range order (Fig. 14b) whereas other particles demonstrate structures with layered carbon planes, rings, or folded ribbons (Fig 14c). The particles generated at 532 nm are smaller and more elongated than those formed at similar fluences with 1064-nm irradiation, and the morphology is similar to that of particles formed with high-fluence irradiation (Fig. 6). At higher fluences, however, fewer particles have regions of long-range order, and particles such as that shown in Fig. 14c were not seen at higher fluences.

NEXAFS spectra were recorded for soot particles exposed to 532-nm radiation at laser fluences of 0.01 J/cm^2, 0.05 J/cm^2, 0.2 J/cm^2, and 0.8 J/cm^2. At fluences $\leq$ 0.05 J/cm^2, STXM images show no changes in particle morphology, and NEXAFS spectra recorded over 15 different regions from these samples demonstrate no chemical bonding changes with fluence, as shown in Fig. 15. At fluences greater than $\geq$ 0.2 J/cm^2, distinct changes in the number of particles and particle morphology are observed. As noted above, the large branched agglomerates, such as that shown in Fig. 7a, are no longer present. At a laser fluence of 0.2 J/cm^2 and greater, the primary particle structure of aggregates is not discernable in the samples collected for the STXM measurements. Rather, a few individual denser particles (sub-micron in size) are apparent (see Fig. 7b).

Fluence-dependent NEXAFS spectra indicate that a detectable change in the state of carbon hybridization in particles occurs when irradiated at laser fluences between 0.2 and 0.8 J/cm^2 at 532 nm. At 0.8 J/cm^2 this transition is characterized by an apparent decrease in graphitic sp^2-hybridized carbon.[100,103] These changes are represented by the differences between the spectra shown in Fig. 15a and the spectrum shown in Fig. 15c. Only two spectra were recorded for the sample illuminated at 0.2 J/cm^2, and both of these spectra looked like the curve presented in Fig. 15b. These spectra also demonstrate an apparent decrease in graphitic sp^2-hybridized carbon by a reduction in the peak at 285.3 eV. In this case, however, the aromatic carbon peak is shifted by 0.4 eV to a lower energy, which may indicate formation of fullerenic carbon. One striking difference between these spectra and those shown in Figs. 15a and 15c is the appearance of a strong peak at 288.7 eV in conjunction with a decrease in the graphitic carbon, indicating significant contributions from C-H. A single spectrum recorded with the sample irradiated at 0.8 J/cm^2 has similar features and is shown in Fig. 15b. Although a detailed understanding of the mechanism for these spectral changes is beyond the scope of this paper, spectral changes observed in particles irradiated at fluences ≥ 0.2 J/cm^2 support the premise that soot particles are significantly altered by laser irradiation either through formation of new particles or annealing.

C. Effects of 532- Versus 1064-nm Radiation on New Particle Formation

New particle formation was measured using the SMPS at 532 and 1064 nm. More new particle production occurred with the shorter wavelength. The number of new particles produced per aggregate is shown in Fig. 11c (left axis). As noted above, the onset of observable nanoparticle production (at which the concentration of small-mode particles is ~1% of the original particle concentration) occurs at ~0.12 J/cm^2 at 532 nm and at ~0.22 J/cm^2 at 1064 nm. The yield of new

particles is higher at 532 nm than at 1064 nm at all fluences above 0.12 J/cm^2. At 532 nm the yield reaches a plateau at fluences greater than ~0.5 J/cm^2; such a plateau was not observed at 1064 nm at the fluences used in this study. The yield of new particles is comparable for the two wavelengths at the highest fluences (>0.75 J/cm^2). This dependence on fluence is similar to the observations of Stipe et al.[42] at 193 nm. In their work, however, the onset of new particle production occurred at ~0.07 J/cm^2, and small-mode particle growth became saturated at 0.17 J/cm^2. These fluences are substantially lower than the corresponding values reported here for longer wavelengths.

5. Discussion

The results of calculations of the fractional amount of volatilized carbon mass for 532-nm laser heating are shown in Figure 11c (right axis). The amount of volatilized carbon was integrated from 0 to 150 ns, at which point mass loss by sublimation and photodesorption has ceased. Although the model does not currently include laser excitation at wavelengths other than 532 nm, carbon volatilization is expected to be less efficient at 1064 than at 532 nm for two reasons: (1) the absorption coefficient is inversely correlated with wavelength (proportional to $\lambda^{-0.83}$ according to the RDG approximation) and is thus much lower at 1064 nm, and (2) the efficiency of photodesorption is lower at 1064 nm, assuming a 2-photon transition at 532 nm and a 3- or 4-photon process at 1064 nm. The calculated increase in mass loss with fluence at 532 nm is more gradual than the increase in the number of new particles. The model indicates an earlier onset of substantial mass loss and does not reach a plateau until ~1.5 J/cm^2 when the particle has been completely vaporized. New particle production via nucleation will depend on condensation rates, which are not included in the model. The experimental and modeling results shown here are thus not directly comparable, but they indicate that vaporization of the particle could generate

sufficient gas-phase carbon species to account for the observed new particle formation by recondensation at these fluences.

Small carbon clusters (predominantly C, C_2, and C_3) may thus sublime or photodesorb from soot aggregates and homogeneously nucleate to form new particles. This mechanism is consistent with observations of laser-induced particle production from graphite, particularly at wavelengths in the visible[65,74,77-79] and infrared[53,64,75,76] regions at ambient pressures above 1 Torr or in free jet expansions into vacuum. Previous work on graphite has shown that small carbon clusters can react to form larger clusters,[53-56,81] which can then act as nucleation sites for particle growth. As indicated by the combined results of TEM images, STXM images, and NEXAFS spectra, this process leads to apparent changes in the sp^2 hybridization. These particles may partially anneal to form small regions with more ordered structure. Alternatively, under some conditions, surface ablation of the primary particle may produce graphitic fragments, which then serve as nucleation sites for new particle formation. Vaporization of such crystallites from graphite with semi-isolated graphite platelets has been hypothesized as a mechanism for generation of large carbon clusters.[114]

The larger aggregates do not appear to be effective sites for heterogeneous cluster nucleation, e.g., the large regions of disordered carbon in Figure 6 are not apparent on the aggregate in Figure 5. At all fluences above the threshold for new particle formation, the median size of the large-mode aggregates is smaller than that of the non-irradiated particles, as shown in Fig. 11a. A possible explanation is that at such high fluences the particles become superheated, pressure and temperature gradients are established at the surface, and convective transport of carbon clusters away from the surface leads to a supersonic expansion.[84,88] These pressure waves and large flux of carbon away from the surface hinder transport of clusters back to the

surface and reduce the rate of cluster recondensation on the original aggregate. Figure 11a also shows a growth in the median diameter of the large-mode aggregates with fluence following a minimum at intermediate fluences, suggesting that some amount of recondensation may occur when the cluster concentration is very high. Caution should be used in drawing such conclusions from these data, however, because this behavior of the large-mode median size and the anti-correlated behavior of the number of large-mode particles may be an artifact of the fitting procedure. Uncertainties in these parameters are more significant for the large-mode, for which the distribution was truncated. In addition, if significant recondensation were occurring on large-mode aggregates, TEM images showing material with no long-range order coating the aggregates might be expected but was not observed.

Our conclusions are consistent with those of Dasch,[34] Witze et al.,[35] and Yoder et al.[36] who measured changes in scattering and absorption cross sections during laser irradiation of soot and hypothesized that particle size reduction at fluences above 0.2 J/cm^2 occurred by vaporization of the particle. Our conclusions are also consistent with those of Vander Wal et al.[29-32] who deduced from TEM images of laser-irradiated soot that aggregates do not disaggregate into primary particles upon laser irradiation but at high fluences lose mass via vaporization of primary particles.

Our results suggest that complete disaggregation of the aggregate into primary particles followed by re-aggregation does not occur. Such disaggregation and re-aggregation would likely lead to significant changes in the electric-mobility aggregate size distribution, which we do not observe. In addition, the small-mode component does not have the same physical and chemical structure as the original primary particles and increases in size with laser fluence, suggesting that, if disaggregation and re-aggregation took place, it would have to be accompanied by a

mechanism such as vaporization and recondensation. Some fragmentation of large aggregates into sections larger than a primary particle may occur, however, which might explain the decrease in median size (Fig. 11a) accompanied by an increase in total number concentration (Fig. 11b) of the large-mode distribution at intermediate fluences. This process may be overwhelmed by the effects of vaporization at higher fluences. Our conclusions are thus inconsistent with those of Filippov et al.[24] who proposed that, during laser irradiation, thermionic emission causes sufficient electrostatic repulsion between primary particles to lead to complete disaggregation of the particle. The mechanism proposed by Filippov et al.[24] is also inconsistent with strong evidence that combustion-generated soot aggregates are held together by covalent bonds between primary particles, rather than by van der Waals forces.[3,7]

Our measurements of new particle formation are inconsistent with those of Kock et al.[33] who recorded particle electric mobility size distributions of laser-irradiated soot and did not observe new particle formation. They used fluences in the range of 0.1-0.6 J/cm^2 at 1064 nm, for which we measure significant nanoparticle generation. Krüger et al.[37] also did not observe new particle formation upon laser irradiation of soot in similar experiments, but their laser fluence (0.12 J/cm^2 at 532 nm) was approximately at our measured threshold for new particle generation, where our observations suggest that new particles are just starting to be observable with an SMPS.

6. Conclusions

We have demonstrated the formation of carbonaceous nanoparticles during pulsed laser irradiation of soot at 532 and 1064 nm. New particles are produced at fluences above ~0.12 J/cm^2 at 532 nm and ~0.22 J/cm^2 at 1064 nm (Fig. 11). The mean size and number density of these new particles, as measured by SMPS, increase with increasing fluence (Fig. 11). At high

fluences (>0.3 J/cm^2 for 532-nm irradiation, >0.5 J/cm^2 for 1064-nm irradiation) new particle formation is accompanied by a decrease in number concentration of large-mode aggregates (Fig. 11b). At intermediate fluences an increase in large-mode aggregate number concentration is accompanied by a decrease in large-mode median size, which may indicate that some fraction of the large aggregates break apart into fragments larger than a primary particle. At higher fluences an increase in the large-mode median diameter and decrease in large-mode number concentration with fluence may indicate recondensation of volatile carbon on the aggregates at high carbon cluster concentrations.

NEXAFS spectra show that the non-irradiated particles are predominantly graphitic sp^2-hybridized carbon and that particles irradiated at fluences above the threshold exhibit significant changes in this peak intensity (Fig. 8). In TEM images small (~30 nm diameter) particles produced by irradiation of soot consist of extended regions without any obvious long-range order and smaller isolated regions of carbon with significant long-range order (Figs. 6 and 14). These ordered regions contain small graphite crystallites or partially annealed carbon that forms small, layered carbon rings or ribbons. Large particles (~100 nm diameter) irradiated at fluences above the threshold fluence consist of primary particles that appear to be similar in size and structure to the non-irradiated primary particles (Fig. 5b). These large particles can also include primary particles with denser layered carbon rings (Fig. 5c), which may result from partial annealing. STXM images suggest that these irradiated aggregates are smaller and denser than the non-irradiated particles (Fig. 7).

These results suggest that particle growth proceeds through recondensation of small carbon clusters (e.g., C, C_2, and C_3) by homogeneous nucleation, heterogeneous nucleation onto graphitic fragments of primary particles, or a combination of both homogeneous and

heterogeneous nucleation. Nanoparticle growth via homogeneous or heterogeneous nucleation of small carbon clusters is consistent with model predictions of the onset and extent of carbon volatilization by sublimation and photodesorption mechanisms. Reduced efficiency of particle formation at 1064 nm over 532 nm is likely due to a smaller absorption coefficient and lower photodesorption efficiency at the longer wavelength. These results are consistent with previous studies of laser irradiation of soot particles and bulk graphite.

Laser-induced vaporization of soot particles and the resulting new particle formation could have significant implications for implementation of laser-induced incandescence for soot detection. For volume fraction measurements, LII is frequently performed at the fluences above the threshold for new particle formation. These results demonstrate that fluences as low as 0.12 J/cm^2 at 532 nm could lead to non-negligible mass loss of the irradiated particle and suggest that particle size measurements using LII and laser-based scattering and extinction measurements of soot particles should be confined to fluences well below this fluence. Morphology and fine structure do not appear to be strongly influenced by irradiation at fluences below the threshold value for new particle formation.

Acknowledgements

The work performed at Sandia was supported by the Division of Chemical Sciences, Geosciences, and Biosciences, the Office of Basic Energy Sciences (BES), the U.S. Department of Energy (DOE). Sandia is a multi-program laboratory operated by Sandia Corporation, a Lockheed Martin Company, for the National Nuclear Security Administration under contract DE-AC04-94-AL85000. We thank Michael Gershenzon for his considerable contributions to the paper, Matt Boisselle for technical support, Pete Witze for stimulating discussions, and Laurence Garvie for helpful suggestions for improving this manuscript. The work at the Advanced Light

Source (ALS) of Lawrence Berkeley National Laboratory (LBNL) was supported by the DOE, BES, the Division of Chemical Sciences, Geosciences, and Biosciences and the Division of Materials Sciences under Contract No. DE-AC03-76S00098. M. K. Gilles and A. V. Tivanski thank A. D. Kilcoyne and T. Tyliszczak for support at beamlines 5.3.2 and 11.0.2, respectively. M. K. Gilles and A. V. Tivanski acknowledge funding from the DOE, Office of Science, Atmospheric Science Program. We gratefully acknowledge the use of facilities within the Center for Solid State Science at Arizona State University (ASU). The work at ASU was funded by the National Science Foundation under grant ATM-0531926.

References

1. J. Lahaye, and G. Prado, "Morphology and internal structure of soot and carbon blacks," in *Particulate carbon: Formation during combustion*, S. D.C., and G. W. Smith, eds. (Plenum, New York, 1981), pp. 33-35.

2. Ü. Ö. Köylü, and G. M. Faeth, "Structure and overfire soot in buoyant turbulent diffusion flames at long residence times," Combust. Flame **89**, 140-156 (1992).

3. H. X. Chen, and R. A. Dobbins, "Crystallogenesis of particles formed in hydrocarbon combustion," Combust. Sci. Technol. **159**, 109-128 (2000).

4. B. Hu, B. Yang, and Ü. Ö. Köylü, "Soot measurements at the axis of an ethylene/air non-premixed turbulent jet flame," Combust. Flame **134**, 93-106 (2003).

5. R. L. Vander Wal, T. M. Ticich, and A. B. Stephens, "Can soot primary particle size be determined using laser-induced incandescence?," Combust. Flame **116**, 291-296 (1999).

6. L. H. van Poppel, H. Friedrich, J. Spinsby, S. H. Chung, J. H. Seinfeld, and P. R. Buseck, "Electron tomography of nanoparticle clusters and implications for atmospheric lifetimes and radiative forcing of soot," Geophys. Res. Lett. **32**, L24811 (2005).

7. J. Lahaye, and F. Ehrburger-Dolle, "Mechanisms of carbon black formation: Correlation with the morphology of aggregates," Carbon **32**, 1319-1324 (1994).

8. T. L. Farias, M. G. Carvalho, Ü. Ö. Köylü, and G. M. Faeth, "Computational evaluation of approximate Rayleigh-Debye-Gans/Fractal-Aggregate theory for the absorption and scattering properties of soot," J. Heat Transfer **117**, 152-159 (1995).

9. T. L. Farias, Ü. Ö. Köylü, and M. G. Carvalho, "Range of validity of the Rayleigh-Debye-Gans theory for optics of fractal aggregates," Appl. Opt. **35**, 6560-6567 (1996).

10. Ü. Ö. Köylü, "Quantitative analysis of in situ optical diagnostics for inferring particle/aggregate parameters in flames: Implications for soot surface growth and total emissivity," Combust. Flame **109**, 488-500 (1996).

11. J. C. Ku, and K.-H. Shim, "A comparison of solutions for light scattering and absorption by aggregated and arbitrarily-shaped particles," J. Quant. Spectrosc. Radiat. Transfer **47**, 201-220 (1992).

12. J. C. Ku, and K.-H. Shim, "Optical diagnostics and radiative properties of simulated soot aggregates," J. Heat Transfer **113**, 953-958 (1991).

13. Ü. Ö. Köylü, and G. M. Faeth, "Fractal and projected structure properties of soot aggregates," Combust. Flame **100**, 621-633 (1995).

14. C. M. Sorensen, "Light scattering by fractal aggregates: A review," Aerosol Sci. Technol. **35**, 648-687 (2001).

15. R. J. Santoro, and C. R. Shaddix, "Laser-Induced Incandescence," in *Applied Combustion Diagnostics*, K. Kohse-Höinghaus, and J. B. Jeffries, eds. (Taylor & Francis, New York, NY, 2002), pp. 252-286.

16. J. A. Pinson, D. L. Mitchell, and R. J. Santoro, "Quantitative, planar soot measurements in a D. I. diesel engine using laser-induced incandescence and light scattering," Proc. SAE, SAE Paper No. 932650 (1993).

17. J. A. Pinson, T. Ni, and T. A. Litzinger, "Quantitative imaging study of the effects of intake air temperature on soot evaluation in an optically-accessible D. I. diesel engine," Proc. SAE, SAE Paper No. 942044 (1994).

18. R. L. Vander Wal, and D. L. Dietrich, "Laser-induced incandescence applied to droplet combustion," Appl. Opt. **34**, 1103-1107 (1995).

19. T. Ni, J. A. Pinson, S. Gupta, and R. J. Santoro, "Two-dimensional imaging of soot volume fraction by the use of laser-induced incandescence," Appl. Opt. **34**, 7083-7091 (1995).

20. B. Mewes, and J. M. Seitzman, "Soot volume fraction and particle size measurements with laser-induced incandescence," Appl. Opt. **36**, 709-717 (1997).

21. P. Roth, and A. V. Filippov, "In situ ultrafine particle sizing by a combination of pulsed laser heatup and particle thermal emission," J. Aerosol Sci. **27**, 95-104 (1996).

22. B. Quay, T.-W. Lee, T. Ni, and R. J. Santoro, "Spatially resolved measurements of soot volume fraction using laser-induced incandescence," Combust. Flame **97**, 384-392 (1994).

23. C. R. Shaddix, and K. C. Smyth, "Laser-induced incandescence measurements of soot production in steady and flickering methane, propane, and ethylene diffusion flames," Combust. Flame **107**, 418-452 (1996).

24. A. V. Filippov, M. W. Markus, and P. Roth, "In situ characterization of ultrafine particles by laser-induced incandescence: Sizing and particle structure determination," J. Aerosol Sci. **30**, 71-87 (1999).

25. K. Inagaki, S. Takasu, and K. Nakakita, "In-cylinder quantitative soot concentration measurement by laser-induced incandescence," Proc. SAE, SAE Paper No. 1999-1901-0508 (1999).

26. S. Schraml, S. Will, and A. Leipertz, "Simultaneous measurement of soot mass concentration and primary particle size in the exhaust of a DI diesel engine by time-resolved laser-induced incandescence," Proc. SAE, SAE Paper No. 1999-1901-0146 (1999).

27. D. J. Bryce, N. Ladommatos, and H. Zhao, "Quantitative investigation of soot distribution by laser-induced incandescence," Appl. Opt. **39**, 5012-5022 (2000).

28. C. Allouis, A. D'Alessio, C. Noviello, and F. Beretta, "Time resolved laser induced incandescence for soot and cenospheres measurements in oil flames," Combust. Sci. Technol. **153**, 51-63 (2000).

29. R. L. Vander Wal, and M. Y. Choi, "Pulsed laser heating of soot: Morphological changes," Carbon **37**, 231-239 (1999).

30. R. L. Vander Wal, C. Y. Choi, and K. O. Lee, "The effects of rapid heating of soot: implications when using laser-induced incandescence for soot diagnostics," Combust. Flame **102**, 200-204 (1995).

31. R. L. Vander Wal, T. M. Ticich, and A. B. Stephens, "Optical and microscopy investigations of soot structure alterations by laser-induced incandescence," Appl. Phys. B **67**, 115-123 (1998).

32. R. L. Vander Wal, and K. A. Jensen, "Laser-induced incandescence: Excitation intensity," Appl. Opt. **37**, 1607-1616 (1998).

33. B. F. Kock, "in preparation," (2006).

34. C. J. Dasch, "Continuous-wave probe laser investigation of laser vaporization of small soot particles in a flame," Appl. Opt. **23**, 2209-2215 (1984).

35. P. O. Witze, S. Hochgreb, D. Kayes, H. A. Michelsen, and C. R. Shaddix, "Time-resolved laser-induced incandescence and laser elastic scattering measurements in a propane diffusion flame," Appl. Opt. **40**, 2443-2452 (2001).

36. G. D. Yoder, P. K. Diwaker, and D. W. Hahn, "Assessment of soot particle vaporization effects during laser-induced incandescence with time-resolved light scattering," Appl. Opt. **44**, 4211-4219 (2005).

37. V. Krüger, C. Wahl, R. Hadef, K. P. Geigle, W. Stricker, and M. Aigner, "Comparison of laser-induced incandescence method with scanning mobility particle sizer technique: The influence of probe sampling and laser heating on soot particle size distribution," Meas. Sci. Technol. **16**, 1477-1486 (2005).

38. C. J. Damm, D. Lucas, R. F. Sawyer, and C. P. Koshland, "Characterization of diesel particulate matter with excimer laser fragmentation fluorescence spectroscopy," Proc. Combust. Inst. **29**, 2767-2774 (2002).

39. P.-E. Bengtsson, and M. Aldén, "Soot-visualization strategies using laser techniques," Appl. Phys. B **60**, 51-59 (1995).

40. C. B. Stipe, B. S. Higgins, D. Lucas, C. P. Koshland, and R. F. Sawyer, "Soot detection using excimer laser fragmentation fluorescence spectroscopy," Proc. Combust. Inst. **29**, 2759-2766 (2002).

41. J. Walewski, M. Rupinski, H. Bladh, Z. S. Li, P.-E. Bengtsson, and M. Aldén, "Soot visualisation by use of laser-induced soot vapourisation in combination with polarisation spectroscopy," Appl. Phys. B **77**, 447-454 (2003).

42. C. B. Stipe, J. H. Choi, D. Lucas, C. P. Koshland, and R. F. Sawyer, "Nanoparticle production by UV irradiation of combustion generated soot particles," J. Nanoparticle Res. **6**, 467-477 (2004).

43. F. Kokai, and Y. Koga, "Time-of-flight mass spectrometric studies on the plume dynamics of laser ablation of graphite," Nucl. Instrum. Methods Phys. Res. **B121**, 387-391 (1997).

44. F. Kokai, "Optical emission spectra from laser ablation of graphite at 266 nm and 1064 nm under a magnetic field," Jpn. J. Appl. Phys. **36**, 3504-3509 (1997).

45. R. W. Dreyfus, R. Kelly, and R. E. Walkup, "Laser-induced fluorescence study of laser sputtering of graphite," Nucl. Instrum. Methods Phys. Res. **B23**, 557-561 (1987).

46. J. J. Gaumet, A. Wakisaka, Y. Shimizu, and Y. Tamori, "Energetics for carbon clusters produced directly by laser vaporization of graphite: Dependence on laser power and wavelength," J. Chem. Soc., Faraday Trans. **89**, 1667-1670 (1993).

47. D. J. Krajnovich, "Laser sputtering of highly oriented pyrolytic graphite at 248 nm," J. Chem. Phys. **102**, 726-743 (1995).

48. H. C. Ong, and R. P. H. Chang, "Effect of laser intensity on the properties of carbon plumes and deposited films," Phys. Rev. B **55**, 13213-13213,13220 (1997).

49. Y. Yamagata, A. Sharma, and J. Narayan, "Comparative study of pulsed laser ablated plasma plumes from single crystal graphite and amorphous carbon targets. Part 1. Optical emission spectroscopy," J. Appl. Phys. **88**, 6861-6867 (2000).

50. P. T. Murray, and D. T. Peeler, "Dynamics of graphite photoablation: Kinetic energy of the precursors to diamond-like carbon," Appl. Surf. Sci. **69**, 225-230 (1993).

51. M.-A. Bratescu, Y. Sakai, D. Yamaoka, Y. Suda, and H. Sugawara, "Electron and excited particle densities in a carbon ablation plume," Appl. Surf. Sci. **197-198**, 257-262 (2002).

52. T. Shinozaki, T. Ooie, T. Yano, J. P. Zhao, Z. Y. Chen, and M. Yoneda, "Laser-induced optical emission of carbon plume by excimer and Nd:YAG laser irradiation," Appl. Surf. Sci. **197-198**, 263-267 (2002).

53. F. Kokai, K. Takahashi, M. Yudasaka, and S. Iijima, "Emission imaging spectroscopic and shadowgraphic studies on the growth dynamics of graphitic carbon particles synthesized by CO_2 laser vaporization," J. Phys. Chem. B **103**, 8686-8693 (1999).

54. T. Moriwaki, M. Kobayashi, M. Osaka, M. Ohara, H. Shiromaru, and Y. Achiba, "Dual pathway of carbon cluster formation in the laser vaporization," J. Chem. Phys. **107**, 8927-8932 (1997).

55. K. Sasaki, T. Wakabayashi, S. Matsui, and K. Kadota, "Distributions of C_2 and C_3 radical densities in laser-ablation carbon plumes measured by laser-induced fluorescence imaging spectroscopy," J. Appl. Phys. **91**, 4033-4039 (2002).

56. K. Shibagaki, T. Kawashima, K. Sasaki, and K. Kadota, "Formation of positive and negative carbon cluster ions in the initial phase of laser ablation in vacuum," Jpn. J. Appl. Phys. **39**, 4959-4963 (2000).

57. M. Ullmann, S. K. Friedlander, and A. Schmidt-Ott, "Nanoparticle formation by laser ablation," J. Nanoparticle Res. **4**, 499-509 (2002).

58. R. M. Mayo, J. W. Newman, Y. Yamagata, A. Sharma, and J. Narayan, "Comparative study of pulsed laser ablated plasma plumes from single crystal graphite and amorphous carbon targets: Part II. Electrostatic probe measurements," J. Appl. Phys. **88**, 6868-6874 (2000).

59. H. Kamezaki, K. Tokunaga, S. Fukuda, N. Yoshida, and T. Muroga, "Pulse high heat flux experiment with laser beams on graphite," J. Nucl. Mater. **179**, 193-196 (1991).

60. K. A. Lincoln, and M. A. Covington, "Dynamic sampling of laser-induced vapor plumes by mass spectrometry," Int. J. Mass Spectrom. Ion Phys. **16**, 191-208 (1975).

61. T. Wakabayashi, T. Momose, and T. Shida, "Mass spectroscopic studies of laser ablated carbon clusters as studied by photoionization with 10.5 eV photons under high vacuum," J. Chem. Phys. **111**, 6260-6263 (1999).

62. J. Berkowitz, and W. A. Chupka, "Mass spectrometric study of vapor ejected from graphite and other solids by focused laser beams," J. Chem. Phys. **40**, 2735-2736 (1964).

63. P. Monchicourt, "Onset of carbon cluster formation inferred from light emission in a laser-induced expansion," Phys. Rev. Lett. **66**, 1430-1433 (1991).

64. K. Sasaki, T. Wakasaki, and K. Kadota, "Observation of continuum optical emission from laser ablation carbon plumes," Appl. Surf. Sci. **197-198**, 197-201 (2002).

65. E. A. Rohlfing, "Optical emission studies of atomic, molecular, and particulate carbon produced from a laser vaporization cluster source," J. Chem. Phys. **89**, 6103-6112 (1988).

66. M. Anselment, R. S. Smith, E. Daykin, and L. F. Dimauro, "Optical emission studies on graphite in a laser/vaporization supersonic jet cluster source," Chem. Phys. Lett. **134**, 444-449 (1987).

67. E. A. Rohlfing, D. M. Cox, and A. Kaldor, "Production and characterization of supersonic carbon cluster beams," J. Chem. Phys. **81**, 3322-3330 (1984).

68. M. Jeunehomme, and R. P. Schwenker, "Focused laser-beam experiment and the oscillator strength of the Swan system," J. Chem. Phys. **42**, 2406-2408 (1965).

69. A. M. Keszler, and L. Nemes, "Time averaged emission spectra of Nd:YAG laser induced carbon plasmas," J. Mol. Struct. **695-696**, 211-218 (2004).

70. J. A. Howe, "Observations on the maser-induced graphite jet," J. Chem. Phys. **39**, 1362-1363 (1963).

71. L. Nemes, A. M. Keszler, J. O. Hornkolh, and C. G. Parigger, "Laser-induced carbon plasma emission spectroscopic measurements on solid targets and in gas-phase optical breakdown," Appl. Opt. **44**, 3661-3667 (2005).

72. S. S. Harilal, R. C. Isaac, C. V. Bindhu, V. P. N. Nampoori, and C. P. G. Vallabhan, "Optical emission studies of C2 species in laser-produced plasma from carbon," J. Phys. D: Appl. Phys. **30**, 1703-1709 (1997).

73. A. O'Keefe, M. M. Ross, and A. P. Baronavski, "Production of large carbon cluster ions by laser vaporization," Chem. Phys. Lett. **130**, 17-19 (1986).

74. G. F. Lorusso, V. Capozzi, P. Milani, A. Minafra, and D. Lojacono, "UV spectra of graphite microparticles produced by laser vaporization," Solid State Commun. **85**, 729-734 (1993).

75. F. Kokai, K. Takahashi, D. Kasuya, A. Nakayama, Y. Koga, M. Yudasaka, and S. Iijima, "Laser vaporization synthesis of polyhedral graphite," Appl. Phys. A **77**, 69-71 (2003).

76. S. M. Kimbrell, and E. S. Yeung, "Real-time particle size measurements in laser-generated plumes by Mie scattering," Appl. Spectrosc. **43**, 1248-1251 (1989).

77. S. Iijima, T. Wakabayashi, and Y. Achiba, "Structures of carbon soot prepared by laser ablation," J. Phys. Chem. **100**, 5839-5843 (1996).

78. T. Ishigaki, S. Suzuki, H. Kataura, W. Krätschmer, and Y. Achiba, "Characterization of fullerenes and carbon nanoparticles generated with a laser-furnace technique," Appl. Phys. A **70**, 121-124 (2000).

79. E. A. Rohlfing, and D. W. Chandler, "Two-color pyrometric imaging of laser-heated carbon particles in a supersonic flow," Chem. Phys. Lett. **170**, 44-50 (1990).

80. H. W. Kroto, J. R. Heath, S. C. O'Brien, R. F. Curl, and R. E. Smalley, "C_{60}: Buckminsterfullerene," Nature **318**, 162-163 (1985).

81. D. M. Cox, K. C. Reichmann, and A. Kaldor, "Carbon clusters revisited: The "special" behavior of C_{60} and large carbon clusters," J. Chem. Phys. **88**, 1588-1597 (1988).

82. M. Pellarin, E. Cottancin, J. Lermé, J. L. Vialle, and M. Broyer, "Coating and polymerization of C_{60} with carbon: A gas phase photodissociation study," J. Chem. Phys. **117**, 3088-3097 (2002).

83. S. Suzuki, H. Yamagachi, R. Sen, H. Kataura, W. Krätschmer, and Y. Achiba, "Time and space evolution of carbon species generated with a laser furnace technique," AIP Conf. Proc. **590**, 51-54 (2001).

84. H. A. Michelsen, P. O. Witze, D. Kayes, and S. Hochgreb, "Time-resolved laser-induced incandescence of soot: The influence of experimental factors and microphysical mechanisms," Appl. Opt. **42**, 5577-5590 (2003).

85. http://rsb.info.nih.gov/ij/, "Image processing and analysis in Java."

86. A. L. D. Kilcoyne, T. Tyliszczak, W. F. Steele, S. Fakra, P. Hitchcock, K. Franck, E. Anderson, B. Harteneck, E. G. Rightor, G. E. Mitchell, A. P. Hitchcock, L. Yang, T. Warwick, and H. Ade, "Interferometer-controlled scanning transmission X-ray microscopes at the Advanced Light Source," J. Synchrotron Radiat. **10**, 125-136 (2003).

87. Y. Ma, C. T. Chen, G. Meigs, K. Randall, and F. Sette, "High-resolution K-shell photoabsorption measurements of simple molecules," Phys. Rev. A **44**, 1848-1858 (1991).

88. H. A. Michelsen, "Understanding and predicting the temporal response of laser-induced incandescence from carbonaceous particles," J. Chem. Phys. **118**, 7012-7045 (2003).

89. A. V. Filippov, M. Zurita, and D. E. Rosner, "Fractal-like aggregates: Relation between morphology and physical properties," J. Colloid Interface Sci. **229**, 261-273 (2000).

90. F. Liu, G. J. Smallwood, and D. R. Snelling, "Effects of primary particle diameter and aggregate size distribution on the temperature of soot particles heated by pulsed lasers," J. Quant. Spectrosc. Radiat. Transfer **93**, 301-312 (2005).

91. D. R. Snelling, F. Liu, G. J. Smallwood, and Ö. L. Gülder, "Determination of the soot absorption function and thermal accommodation coefficient using low-fluence LII in a laminar coflow ethylene diffusion flame," Combust. Flame **136**, 180-190 (2004).

92. J. H. Seinfeld, and S. N. Pandis, *Atmospheric Chemistry and Physics from Air Pollution to Climate Change* (John Wiley and Sons, New York, 1998).

93. T. T. Charalampopoulos, and H. Chang, "Agglomerate parameters and fractal dimension of soot using light scattering-Effects of surface growth," Combust. Flame **87**, 89-99 (1991).

94. Ü. Ö. Köylü, Y. C. Xing, and D. E. Rosner, "Fractal morphology analysis of combustion-generated aggregates using angular light scattering and electron microscope images," Langmuir **11**, 4848-4854 (1995).

95. J.-S. Wu, S. S. Krishnan, and G. M. Faeth, "Refractive indices at visible wavelengths of soot emitted from buoyant turbulent diffusion flames," J. Heat Transfer **119**, 230-237 (1997).

96. W. S. Bacsa, W. A. de Heer, D. Ugarte, and A. Châtelain, "Raman spectroscopy of closed-shell carbon particles," Chem. Phys. Lett. **211**, 346-352 (1993).

97. R. H. Hurt, G. P. Crawford, and H.-S. Shim, "Equilibrium nanostructure of primary soot particles," Proc. Combust. Inst. **28**, 2539-2546 (2000).

98. R. L. Vander Wal, "A TEM methodology for the study of soot particle structure," Combust. Sci. Technol. **126**, 333-357 (1997).

99. T. Ishiguro, Y. Takatori, and K. Akihama, "Microstructure of diesel soot particles probed by electron microscopy: First observation of inner core and outer shell," Combust. Flame **108**, 231-234 (1997).

100. M. S. Dresselhaus, G. Dresselhaus, and P. C. Eklund, *Science of Fullerenes and Carbon Nanotubes* (Academic Press, San Diego, 1996).

101. J. Robertson, "Amorphous carbon," Adv. Phys. **35**, 317-374 (1986).

102. R. Gago, I. Jiménez, and J. M. Albella, "Detecting with X-ray absorption spectroscopy the modifications of the bonding structure of graphitic carbon by amorphisation, hydrogenation and nitrogenation," Surf. Sci. **482-485**, 530-536 (2001).

103. R. Gago, M. Vinnichenko, H. U. Jäger, A. Y. Belov, I. Jiménez, N. Huang, H. Sun, and M. F. Maitz, "Evolution of sp^2 networks with substrate temperature in amorphous carbon films: Experiment and theory," Phys. Rev. B **72**, 014120 (2005).

104. B. L. Henke, P. Lee, T. J. Tanaka, R. L. Shimabukuro, and B. K. Fuikawa, "Low-energy X-ray interaction coefficients: Photoabsorption, scattering, and reflection - E=100-2000 eV, Z=1-94," At. Data Nucl. Data Tables **27**, 1-144 (1982).

105. R. A. Rosenberg, P. J. Love, and V. Rehn, "Polarization-dependent C(K) near-edge x-ray-absorption fine structure of graphite," Phys. Rev. B **33**, 4034-4037 (1986).

106. C. Lenardi, M. Marino, E. Barborini, P. Piseri, and P. Milani, "Evaluation of hydrogen chemisorption in nanostructured carbon films by near edge X-ray absorption spectroscopy," Eur. Phys. J. B **46**, 441-447 (2005).

107. R. Ahuja, P. A. Brühwiler, J. M. Wills, B. Johansson, N. Mårtensson, and O. Eriksson, "Theoretical and experimental study of the graphite 1s x-ray absorption edges," Phys. Rev. B **54**, 14396-14404 (1996).

108. R. F. Willis, B. Fitton, and G. S. Painter, "Secondary-electron emission spectroscopy and the observation of high-energy excited states in graphite: Theory and experiment," Phys. Rev. B **9**, 1926-1937 (1974).

109. F. L. Coffman, R. Cao, P. A. Pianetta, S. Kapoor, M. Kelly, and L. J. Terminello, "Near-edge x-ray absorption of carbon materials for determining bond hybridization in mixed sp^2/sp^3 bonded materials," Appl. Phys. Lett. **69**, 568-570 (1996).

110. J. Stöhr, *NEXAFS Spectroscopy* (Springer, Berlin, 1996).

111. M. B. Fernandes, J. O. Skjemstad, B. B. Johnson, J. D. Wells, and P. Brooks, "Characterization of carbonaceous combustion residues: I. Morphological, elemental and spectroscopic features," Chemosphere **51**, 785-795 (2003).

112. M. B. Fernandes, and P. Brooks, "Characterization of carbonaceous combustion residues: II. Nonpolar organic compounds," Chemosphere **53**, 447-458 (2003).

113. G. D. Cody, H. Ade, S. Wirick, G. D. Mitchell, and A. Davis, "Determination of chemical-structural changes in vitrinite accompanying luminescence alteration using C-NEXAFS analysis," Org. Geochem. **28**, 441-455 (1998).

114. Y. P. Yang, P. Xia, A. L. Junkin, and L. A. Bloomfield, "Direct ejection of clusters from nonmetallic solids during laser vaporization," Phys. Rev. Lett. **66**, 1205-1208 (1991).

Table 1. Results of Fits to Particle Size Distributions (solid lines in Fig. 9)

Laser fluence	Large-mode particles			Small-mode particles		
(J/cm^2)	D_1 (nm)	$N_1\times10^6$ (cm^{-3})	σ_1	D_2 (nm)	$N_2\times10^6$ (cm^{-3})	σ_2

0.00	94.0±0.3	9.88±0.05	1.664±0.005	0	0	0
0.21	89.6±0.4	10.9±0.1	1.73±0.01	13.0±0.1	1.89±0.04	1.31±0.01
0.33	86.8±0.4	11.0±0.1	1.75±0.01	19.5±0.1	9.25±0.06	1.42±0.002
0.76	98.2±0.6	8.22±0.2	1.52±0.01	26.0±0.1	16.5±0.1	1.47±0.004

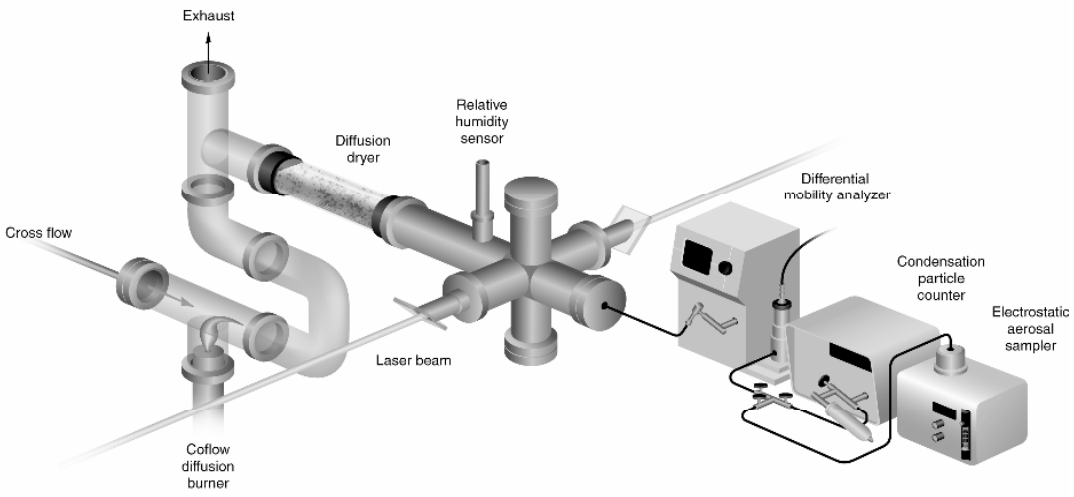

Figure 1. Schematic diagram of the soot flow tube.

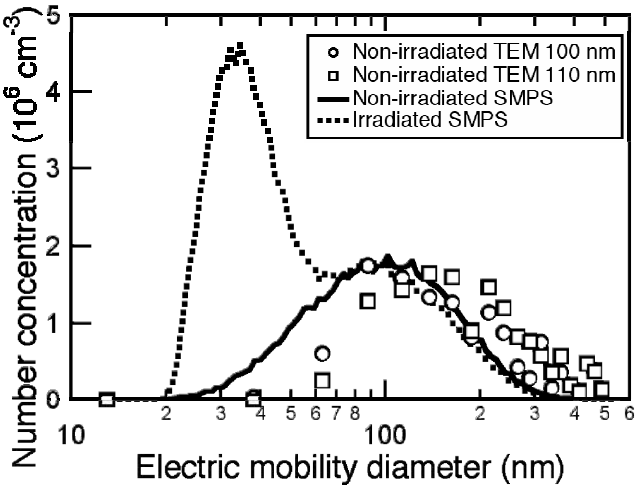

Figure 2. SMPS electric mobility size distributions of non-irradiated soot (solid line) and particles irradiated at 532 nm and 0.7 J/cm^2 (dotted line). Burner flow rates were 0.24 SLM for ethylene, 27.5 SLM for the air coflow, and 65 SLM for the air cross-flow (see text for further details). Symbols represent the average geometric diameters determined from 325 measurements on each of two TEM samples, one collected with the DMA set to a mobility size of 100 nm and the other collected at a mobility size of 110 nm.

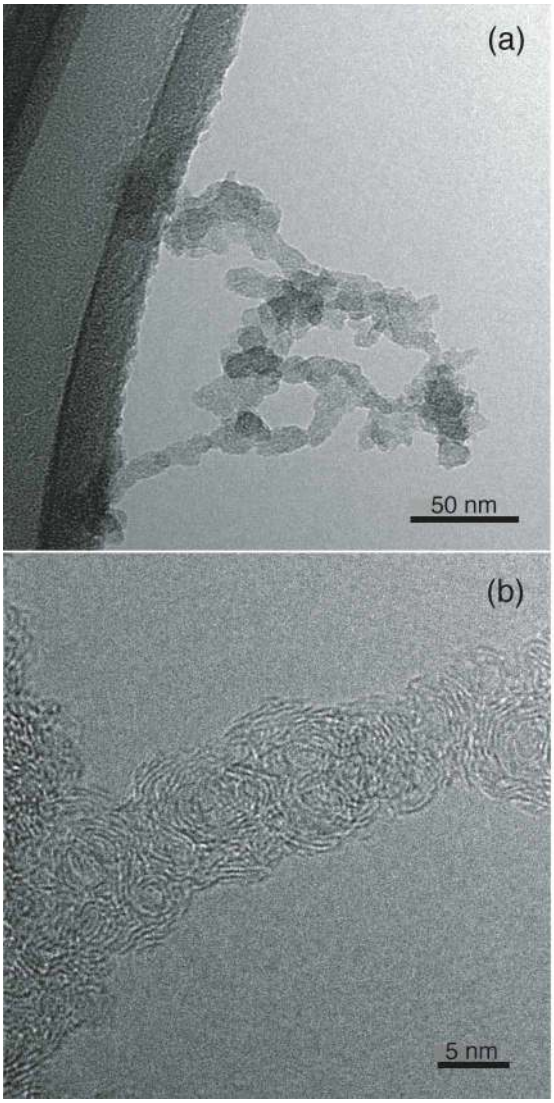

Figure 3. TEM images of non-irradiated soot particles. (a) A soot aggregate from a distribution with a mean geometric diameter of 110(±15) nm and a mean electric mobility diameter of 112(±1) nm. (b) A higher-magnification TEM image of the same particle.

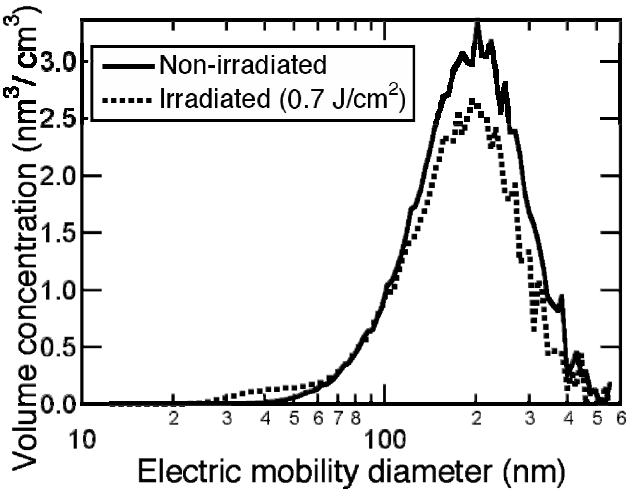

Figure 4. SMPS electric mobility size distributions of irradiated and non-irradiated particles represented as particle volume distributions. The measured number concentrations (Fig. 2) were converted to volume assuming the particles to be spherical with diameters equivalent to the electric mobility diameters. Particles were irradiated at 532 nm with a fluence of 0.7 J/cm^2.

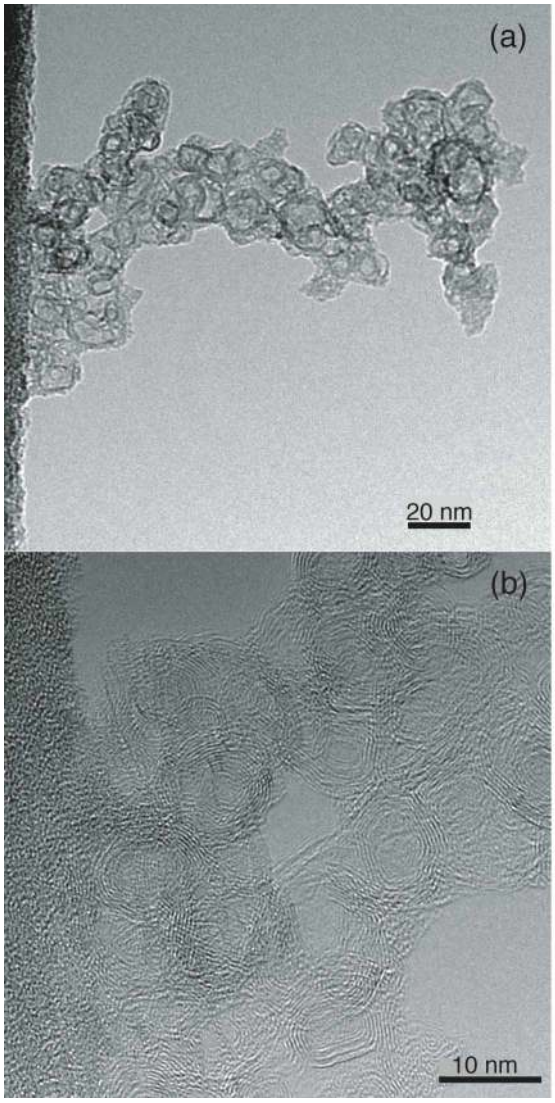

Figure 5. TEM images of a soot particle irradiated at 1064 nm with a fluence of 1 J/cm^2. The particle electric mobility diameter was 100 nm. (a) The aggregate in this TEM image has a branched-chain morphology similar to that of the non-irradiated particles, despite changes in the particle fine structure (b). (b) Higher-magnification TEM image of a part of the same aggregate.

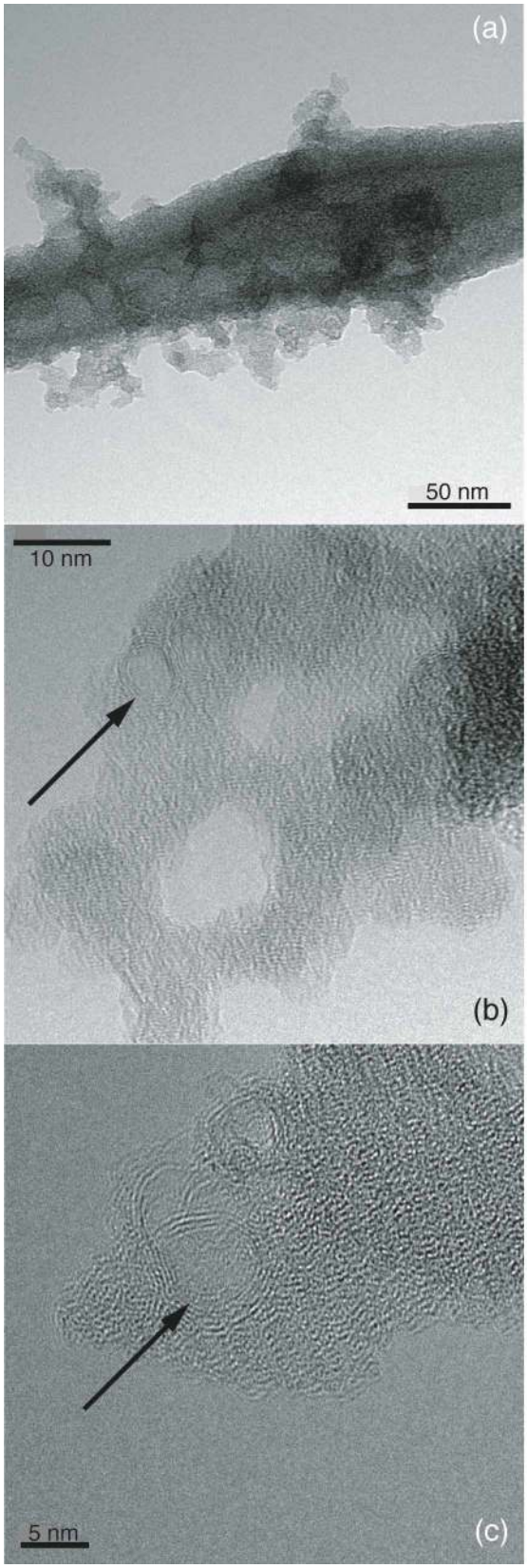
(a)
50 nm
10 nm
(b)
5 nm
(c)

Figure 6. TEM images of soot nanoparticles produced by laser irradiation. Particles were produced at (a) and (b) 1064 nm with a laser fluence of 1 J/cm^2 and (c) 532 nm with a laser fluence of 0.87 J/cm^2 and were collected at an electric mobility diameter of 30 nm. (b) and (c) Higher-magnification TEM images of nanoparticles that appear to be predominantly composed of carbon with no apparent long-range order and that have isolated regions with some long-range order (arrows).

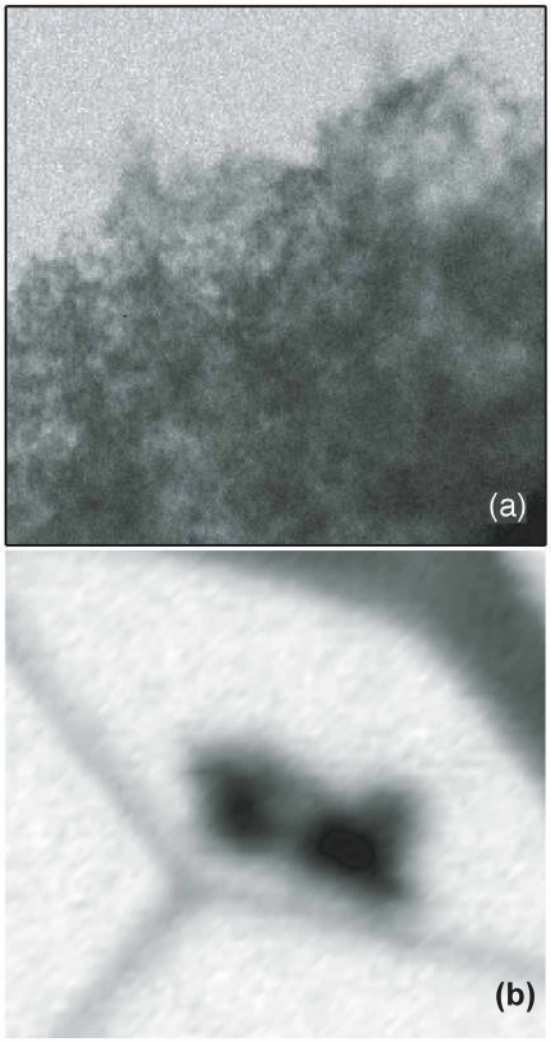

Figure 7. Single-energy images of representative particles imaged by STXM at the carbon edge. (a) Non-irradiated soot imaged with a step size of 60 nm. The image size is 15x15 μm. (b) A soot particle irradiated at 532 nm with a fluence of 0.8 J/cm^2 and imaged with a step size of 30 nm. The image size is 2x2 μm.

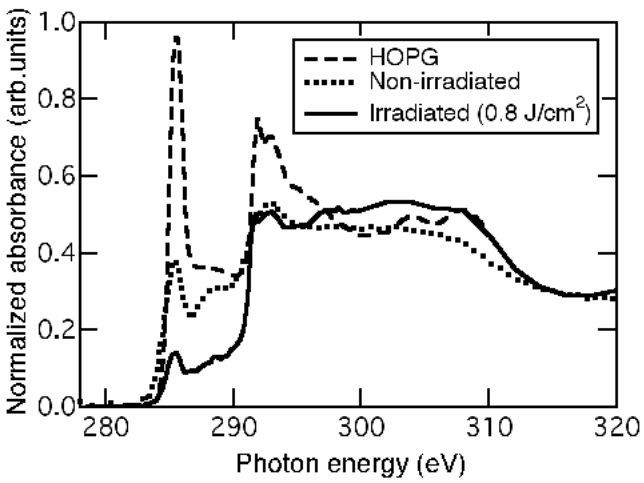

Figure 8. Representative carbon K-edge NEXAFS spectra of soot particles before (dotted line) and after (solid line) laser irradiation with a single laser pulse at 532 nm and a laser fluence of 0.8 J/cm^2. The spectrum of HOPG (dashed line) from Lenardi et al.[106] is provided for comparison.

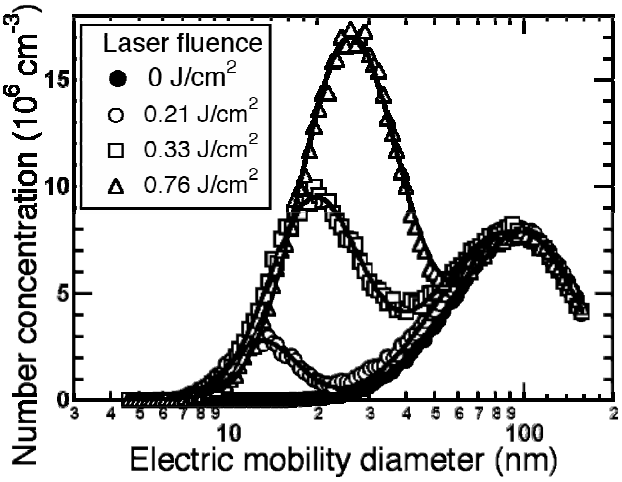

Figure 9. Number concentration of electric mobility size distributions of non-irradiated soot particles (filled circles) and soot irradiated at 532 nm with fluences of 0.21 J/cm^2 (open circles), 0.33 J/cm^2 (squares), and 0.76 J/cm^2 (triangles). The distributions are plotted as $n(\ln D)$. Solid lines are the best fits to the data with a sum of two log-normal distributions, i.e., Eq. (3). The values of fitting parameters are listed in Table 1.

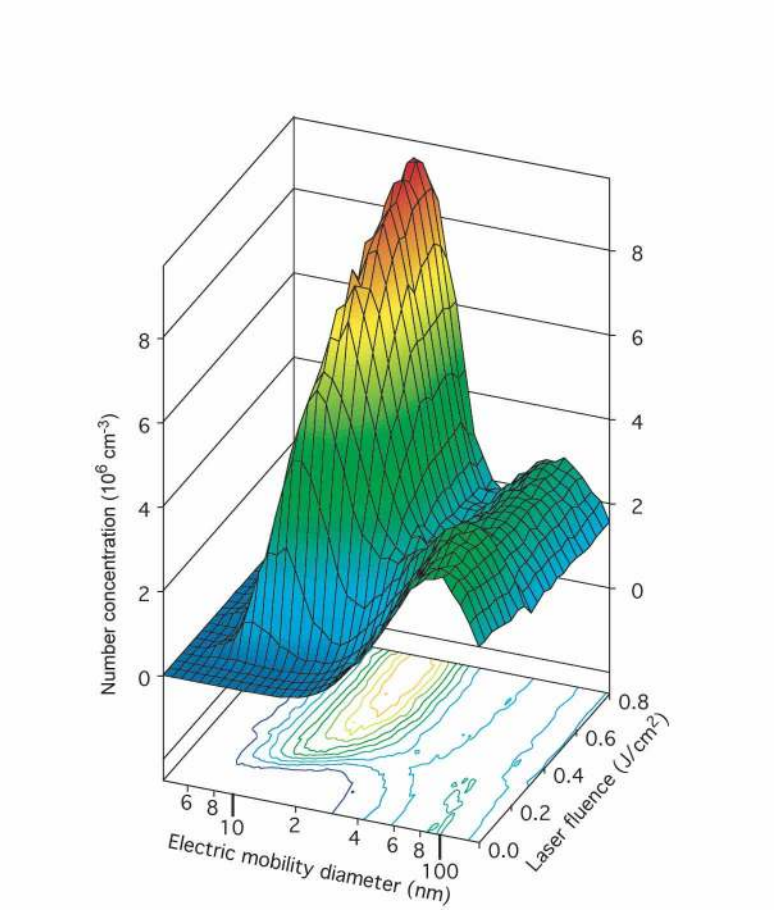

Figure 10. Electric mobility size distributions plotted as a function of laser fluence. Soot was irradiated at 532 nm and sampled with the SMPS. The contour line spacing is 2×10^6 cm^{-3}.

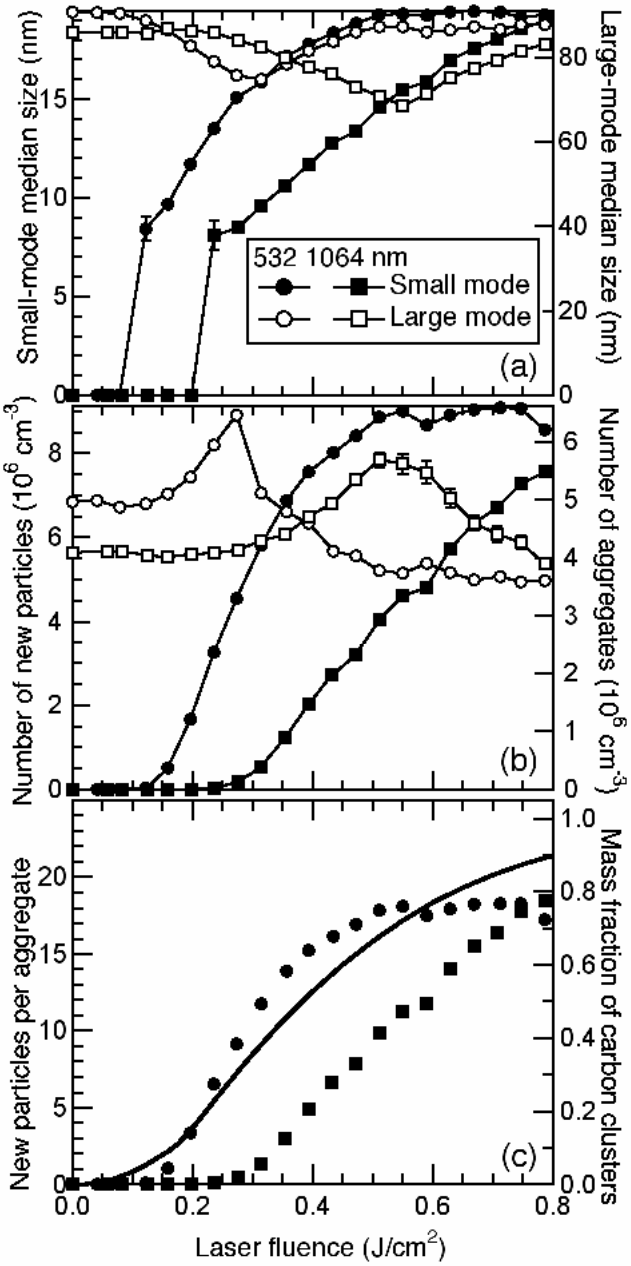

Figure 11. Fluence dependence of median size and number concentration of small-mode and large-mode distributions. Results are shown for 532-nm (circles) and 1064-nm (squares) irradiation. Fits of Eq. (3) to the distributions were used to derive (a) the median particle size (D) for each mode and (b) the total number concentration (N) for each mode. Large-mode results (open symbols) correspond to the right axis, and small-mode results (closed symbols), to

the left axis. (c) Equations (3) and (4) were used to calculate the average number of small particles produced per soot aggregate. The line represents the calculated mass fraction of carbon volatilized into small molecular clusters during 532-nm laser irradiation. Symbols correspond to the left axis; lines correspond to the right axis.

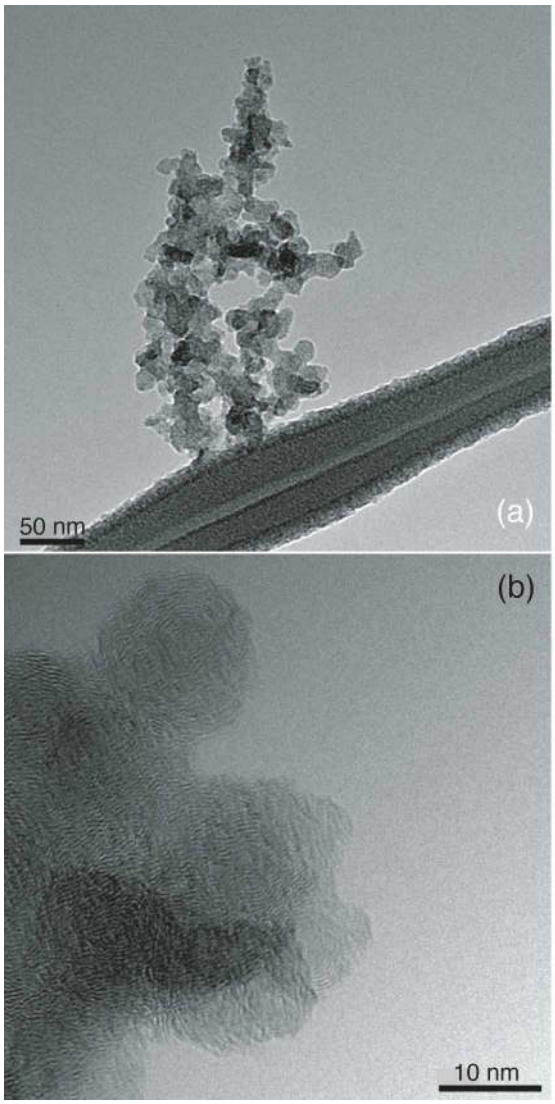

Figure 12. TEM images of a soot particle irradiated at 1064 nm with a fluence of 0.24 J/cm^2. The particle electric mobility diameter was 100 nm. (a) The aggregate in this TEM image has a branched-chain morphology and fine structure similar to that of the non-irradiated particles. (b) Higher-magnification TEM image of a part of the same aggregate.

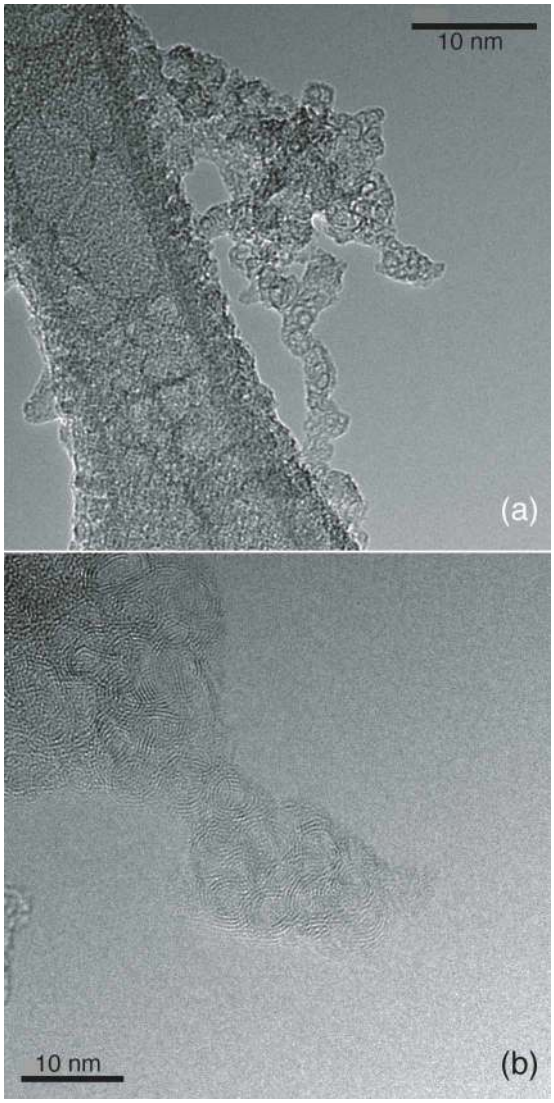

Figure 13. TEM images of a soot particle irradiated at 532 nm with a fluence of 0.3 J/cm^2. The particle electric mobility diameter was 100 nm. (a) The aggregate in this TEM image has a branched-chain morphology similar to that of the non-irradiated particles. (b) Higher-magnification TEM image of a part of the same aggregate.

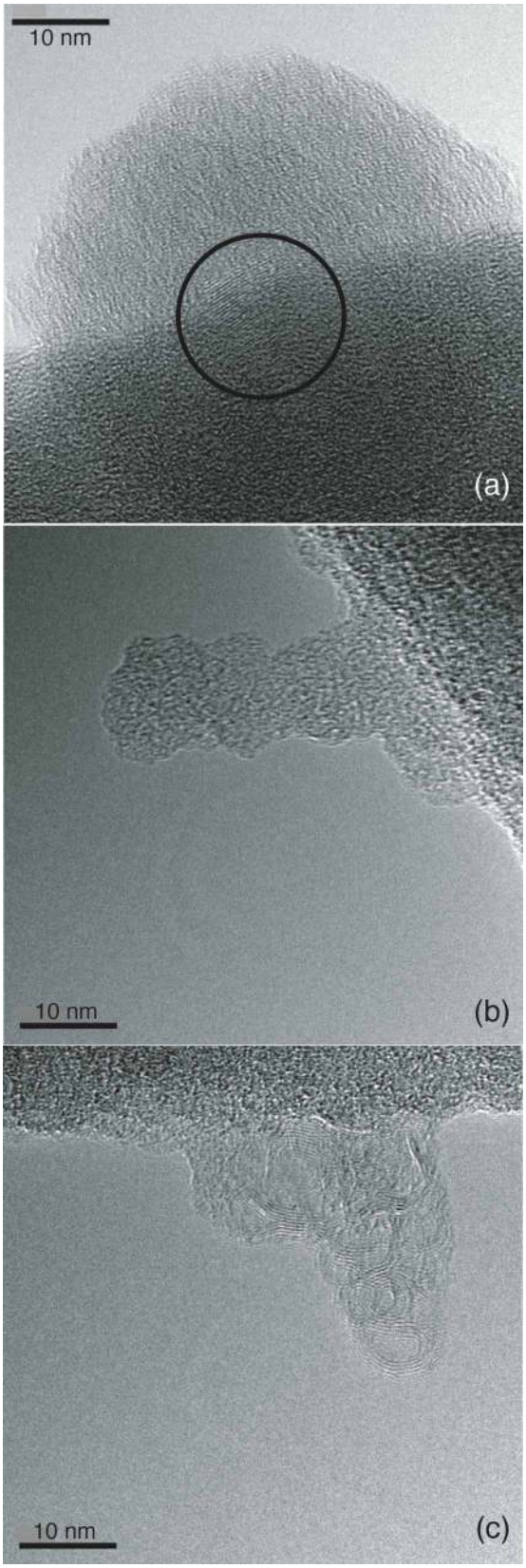
10 nm
(a)
10 nm
(b)
10 nm
(c)

Figure 14. TEM images of small particles produced by laser irradiation of soot. (a) Higher-magnification TEM image of particles produced at 1064 nm with a fluence of 0.24 J/cm^2 and collected at a mobility diameter of 10 nm. The circle highlights an isolated region of turbostratic graphitic structure. (b) and (c) Higher-magnification TEM images of particles produced at 532 nm with a fluence of 0.3 J/cm^2 and collected at a mobility diameter of 28 nm.

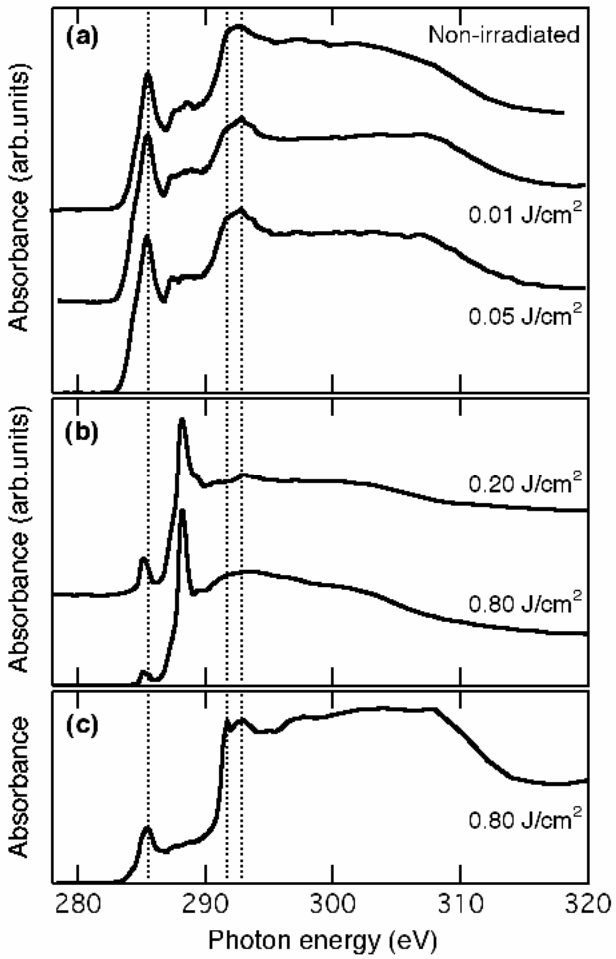

Figure 15. Average carbon K-edge NEXAFS spectra of soot particles (a) before (top line) and after laser irradiation with a single laser pulse at 532 nm and laser fluences of (a) 0.01 J/cm^2, (a) 0.05 J/cm^2, (b) 0.2 J/cm^2, and (b and c) 0.80 J/cm^2, as indicated. The curves have been normalized and offset from one another for clarity. Vertical dotted lines indicate energy levels for the 1s-π* transition of aromatic carbon (285.5 eV), 1s-σ* carbon transition (~292.8 eV), and the exciton peak (291.7 eV).